Monthly Notices of the ROYAL ASTRONOMICAL SOCIETY

MNRAS **533,** 771–794 (2024) https://doi.org/10.1093/mnras/stae1831
Advance Access publication 2024 July 29

Two distinct molecular cloud populations detected in massive galaxies

Tom Rose [1,2★] B. R. McNamara,[1,2] F. Combes,[3] A. C. Edge [4] M. McDonald,[5] Ewan O'Sullivan [6] H. Russell,[7] A. C. Fabian [8] G. Ferland,[9] P. Salomé[3] and G. Tremblay[6]

[1]*Department of Physics and Astronomy, University of Waterloo, Waterloo, ON N2L 3G1, Canada*
[2]*Waterloo Centre for Astrophysics, Waterloo, ON N2L 3G1, Canada*
[3]*LERMA, Observatoire de Paris, PSL Univ., College de France, CNRS, Sorbonne Univ., F-75 014 Paris, France*
[4]*Centre for Extragalactic Astronomy, Durham University, Durham DH1 3LE, UK*
[5]*MIT Kavli Institute, Massachusetts Institute of Technology, 70 Vassar Street, Cambridge, MA 02139, USA*
[6]*Center for Astrophysics | Harvard & Smithsonian, 60 Garden St, Cambridge, MA 01238, USA*
[7]*School of Physics & Astronomy, University of Nottingham, Nottingham NG7 2RD, UK*
[8]*Institute of Astronomy, Cambridge University, Madingley Rd., Cambridge CB3 0HA, UK*
[9]*Department of Physics and Astronomy, University of Kentucky, Lexington, KY 40506-0055, USA*

Accepted 2024 July 23. Received 2024 July 19; in original form 2024 March 6

ABSTRACT

We present new ALMA observations of CO, CN, CS, HCN, and HCO^+ absorption seen against the bright and compact radio continuum sources of eight galaxies. Combined with archival observations, they reveal two distinct populations of molecular clouds, which we identify by combining CO emission and absorption profiles to unambiguously reveal each cloud's direction of motion and likely location. In galaxy discs, we see clouds with low velocity dispersions, low line-of-sight velocities, and a lack of any systemic inflow or outflow. In galactic cores, we find high velocity dispersion clouds inflowing at up to 550 km s^{-1}. This provides observational evidence in favour of cold accretion on to galactic centres, which likely contributes to the fuelling of active galactic nuclei. We also see a wide range in the CO(2-1)/CO(1-0) ratios of the absorption lines. This is likely the combined effect of hierarchical substructure within the molecular clouds and continuum sources which vary in size with frequency.

Key words: galaxies: active – galaxies: clusters: general – radio continuum: galaxies – radio lines: ISM.

1 INTRODUCTION

Our understanding of the molecular gas in the Universe's most massive galaxies has been built upon theory, simulations, and observations (e.g. O'Dea et al. 1994; Pizzolato & Soker 2005; Gaspari et al. 2011; McNamara et al. 2016; Gaspari et al. 2018; Olivares et al. 2019; Rose et al. 2019b; Fabian et al. 2022). Theories can be applied to study molecular gas on a wide range of spatial scales. However, simulations are often limited by computational power, and observations are constrained by telescope capabilities. For observations of extragalactic sources, molecular gas is most readily observed in emission, but this typically limits us to scales of $10^5 M_\odot$ or more. They are therefore orders of magnitude away from resolving cold gas into individual clouds – the scales on which key processes such as star formation and active galactic nucleus (AGN) accretion occur.

An alternative technique to study molecular gas is via absorption lines against a bright and compact background continuum source. This technique is advantageous because its sensitivity is many orders or magnitude higher than emission. As a result, the molecular gas can be studied on much smaller scales. The iconic radio galaxy Centaurus-A was the first system to be studied in this way (Israel et al. 1990). Of particular advantage is that this system's radio continuum emission and absorbing clouds lie within the same galaxy, meaning that any redshifted absorption unambiguously indicates movement towards the galaxy centre along the line of sight. This is in contrast to both emission lines and extrinsic absorption lines (i.e. absorption found due to the chance alignment of a background quasar and an intervening galaxy, e.g. Wiklind & Combes 1996, 1997b). In these cases, there is ambiguity as to whether the observed gas lies in front of or behind the core of the galaxy, so its direction of motion is unclear.

Unfortunately, finding molecular absorption like that in Centaurus-A requires an extremely bright and compact radio continuum source, so a lack of similar observations followed over the next two decades. However, with the much improved angular resolution and sensitivity offered by the Atacama Large Millimeter/submillimeter Array (ALMA), the last decade or so has been more fruitful and many more intrinsic absorption line systems have now been found, mostly in group and cluster environments (e.g. David et al. 2014; Tremblay et al. 2016; Ruffa et al. 2019; Rose et al. 2019a, b, 2020; Kameno et al. 2020). With these advancements, individual cases of molecular and atomic absorption have now been suggested as being due to clouds within the circumnuclear disc and/or accreting on to the central supermassive black hole (e.g. Tremblay et al. 2016; Rose et al. 2019b; Izumi et al. 2023; Morganti et al. 2023; Oosterloo, Morganti & Murthy 2023).

★ E-mail: thomas.rose@uwaterloo.ca

Rose et al. (2019b) presented the first multitarget study of intrinsic molecular absorption with ALMA observations of CO(1-0) and CN(1-0). Added to Centaurus-A, NGC 5044, and Abell 2597, this raised the total number of intrinsic molecular absorption line systems to eight. Initial results from this survey appeared to show that molecular absorption in such galaxies is surprisingly common, with a detection rate of around 40 per cent. Additionally, although most of the absorbing gas clouds had no significant line-of-sight velocity towards or away from their galaxy centre, a slight bias for clouds to be moving towards their galaxy's centre appeared to be present.

Subsequent observations of the edge-on elliptical brightest cluster galaxy Hydra-A have shown that higher order transitions and a wider mix of molecular tracers can be particularly effective at detecting intrinsic molecular absorption (Rose et al. 2020). In this paper we therefore present new ALMA observations of eight galaxies with bright radio continuum sources. The observations cover CO(2-1), CN(2-1), HCO^+(2-1), and HCN(2-1) in many systems with molecular absorption already detected via other lines. These new observations offer a significant improvement – detecting many more molecular absorption regions and with a higher sensitivity. Combined with CO(2-1) observations, we can therefore study the bulk motions of the absorbing clouds in the context of each galaxy's molecular emission. Since the strength and detectability of a galaxy's molecular absorption is proportional to the brightness of the background radio continuum source, most members of our sample are brightest cluster galaxies. Most also contain at least $10^8 M_\odot$ molecular gas.

We try to be exhaustive in studying all known intrinsically absorbing systems. Although a handful of additional intrinsic molecular absorption systems are known, they are without high-resolution observations of the molecular emission. These include Allison et al. (2019), Combes & Gupta (2024), and Emonts et al. (2024). Shortly before the publication of this paper, Tadhunter et al. (2024) have also shown intrinsic molecular absorption in PKS1814–63. The galaxy contains a close to edge-on on molecular gas disc, with narrow absorption features against the central radio continuum. It is therefore consistent with our analysis.

The rest of this paper is laid out as follows. In Section 2 we give details on our sample, and present moments maps and spectra. We also detail our data reduction methods. In Section 3 we calculate excitation temperatures and column densities for the absorbing gas in each system, as well as molecular masses from the emission. In Section 4 we discuss our findings and the potential implications. Section 5 summarizes our findings. We assume Lambda cold dark matter cosmology with $\Omega_M = 0.3$ and $\Omega_\Lambda = 0.7$, and a Hubble constant of $H_0 = 70\,km\,s^{-1}\,Mpc^{-1}$.

2 DATA

2.1 Sample

We present ALMA observations of molecular gas in 12 galaxies. The main details of these observations are given in Table 1, with further technical details available from the ALMA Science Archive. Further information on the location and redshift of each source is given in Table 2, while Table 3 gives each galaxy's classification and summarizes its molecular emission properties. More details on each source's more general properties are given in an online appendix.

The largest set of data we use is from ALMA project 2021.1.00766.S (P.I. Tom Rose), which aimed to detect CO(2-1), CN(2-1), HCO^+(2-1), and HCN(2-1) in several galaxies known to have molecular absorption from other lines. This project followed on from a survey of 23 X-ray-selected brightest cluster galaxies (2017.1.00629.S, P.I. Alastair Edge) which aimed to detect CO(1-0) absorption against the galaxies' radio cores (see Rose et al. 2019b, in which more details on the sample selection can be found). In brief, by selecting the host cluster from its diffuse X-ray emission, this survey was not biased to central galaxies with any particular orientation of their AGNs.

In this paper we aim to provide analysis of the bulk motions of all known intrinsic molecular absorption lines which have complementary high-resolution molecular emission line observations, so data from a number of other projects are also presented. In Table 1, we show the project from which each observation originated. We do not include NGC 1275, which has low significance absorption reported by Nagai et al. (2019). Subsequent IRAM (Institut de Radioastronomie Millimétrique) observations with NOEMA (NOrthern Extended Millimeter Array) at higher sensitivity do not find molecular absorption in this system (project W22CK).

2.2 Data reduction

We produce data cubes from the ALMA observations using measurement sets available from the National Radio Astronomy Observatory (NRAO) Archive. We processed the data with CASA version 6.6.3.22, a software package produced and maintained by NRAO (McMullin et al. 2007). From the measurement sets provided, we made continuum-subtracted images using the CASA tasks `tclean` and `uvcontsub`. In `tclean`, we have used a hogbom deconvolver and produced images with the narrowest possible channel widths. For our moments maps, we use a data cube made with natural weighting to minimize noise. In most cases, we extract our spectra from data cubes made with uniform weighting, which optimizes the angular resolution of the data. This limits contamination from spatially extended molecular emission in the spectra. However, where no detectable emission is present close to the radio core, we extract spectra using a cube made with natural weighting.

The moments maps we show are produced from the CO(2-1) observations of each galaxy, except for Circinus, NGC 1052, and NGC 5044. In Circinus and NGC 1052, we show high angular resolution HCO^+(3-2) and CO(3-2) emission, respectively. In NGC 5044, the CO(2-1) observation has a clear detection of emission, but is of very poor angular resolution. On the other hand, the CO(1-0) observation is less strong, but is of higher angular resolution. We therefore show an intensity map made from the CO(1-0) data, but velocity and velocity dispersion maps made from CO(2-1) data.

We produce our maps using the CASA task `immoments`. Normally moment 0 maps are made using all channel values in each spaxel. However, for sources with a large beam and overlapping emission and absorption, we use 'includepix = [0,100]', i.e. all pixel values from 0 to an arbitrarily large value. This prevents the negative absorption fluxes wiping out positive emission at other velocities. After producing these maps, we therefore estimate the summed value of the remaining positive noise in an emission free region, and subtract it from the whole image. This may bias the overall intensity map to be lower than reality because negative noise will effectively be subtracted from higher significance emission twice. However, this method more accurately displays the emission seen against the radio core. Additionally, this method only affects the moment 0 maps.

Our moments 1 and 2 maps are made with $> 4\,\sigma$ emission, which we find to give the best appearance. To reduce noise in the data cubes,

Table 1. The ALMA observations presented in this paper.

Source	Ang. res. (arcsec)	FOV (arcsec)	Int. time (s)	Obs. date (yyyy-mm-dd)	Line(s)	Cont. flux density (mJy, GHz)	Project code
NGC 6868	0.81	58.8	5100	2018-01-25	CO(1-0)	41, 107	2017.1.00629
NGC 6868	0.11	25	1400	2021-11-20	CO(2-1), CN(2-1)	33, 234	2021.1.00766
NGC 6868	0.16	34.4	2800	2021-11-19	HCO^+(2-1), HCN(2-1)	36, 169	2021.1.00766
Abell S555	0.63	56	2800	2018-01-23	CO(1-0)	32, 103	2017.1.00629
Abell S555	0.14	25.8	3700	2022-07-20	CO(2-1), CN(2-1)	23, 226	2021.1.00766
Abell S555	0.26	33.2	1800	2022-07-05	HCO^+(2-1), HCN(2-1)	25, 175	2021.1.00766
Hydra-A	2.07	57	2700	2018-07-18	CO(1-0)	99, 103	2017.1.00629
Hydra-A	0.26	26	5700	2018-10-30	CO(2-1), CN(2-1)	60, 223	2018.1.01471
Hydra-A	0.34	33.5	5100	2018-11-16	HCO^+(2-1), HCN(2-1)	95, 168	2018.1.01471
Abell 2597	0.43	26	10 900	2013-11-17	CO(2-1)	15, 213	2012.1.00988
Abell 2597	0.17	34.2	2700	2021-11-25	HCO^+(2-1), HCN(2-1)	14, 170	2021.1.00766
Abell 2390	0.40	59.0	8000	2018-01-07	CO(1-0)	22, 98	2017.1.00629
Abell 2390	0.58	30.4	4800	2022-05-20	CO(2-1)	11, 192	2021.1.00766
Abell 2390	0.21	42.1	900	2021-11-22	HCO^+(2-1), HCN(2-1)	14, 138	2021.1.00766
RXCJ0439.0+0520	0.18	29.8	2600	2022-07-22	CO(2-1), CN(2-1)	72, 195	2021.1.00766
RXCJ0439.0+0520	0.30	41.4	1300	2021-12-04	HCO^+(2-1), HCN(2-1)	85,141	2021.1.00766
Abell 1644	1.74	57	2800	2018-08-21	CO(1-0)	67, 103	2017.1.00629
Abell 1644	0.47	25.9	1300	2022-06-08	CO(2-1), CN(2-1)	38, 225	2021.1.00766
Abell 1644	0.19	33.3	1700	2022-07-22	HCO^+(2-1), HCN(2-1)	39, 175	2021.1.00766
Circinus	0.027	16.7	5600	2019-07-14	CO(3-2), HCO^+(4-3), HCN(4-3)	37, 259	2018.1.00581
Circinus	0.020	22.5	5400	2019-06-07	HCO^+(3-2)	29, 350	2018.1.00581
NGC 4261	0.26	24.7	1900	2018-01-19	CO(2-1)	253, 236	2017.1.00301
NGC 4261	0.18	16.8	2300	2018-01-21	CO(3-2), HCO^+(4-3), HCN(4-3)	223, 348	2017.1.01638
NGC 5044	0.74	54	2400	2018-09-20	CO(1-0)	32, 107	2017.1.00629
NGC 5044	1.89	25	1400	2012-01-13	CO(2-1)	45, 228	2011.0.00735
NGC 5044	0.18	34.4	2600	2022-07-22	HCO^+(2-1), HCN(2-1)	38, 170	2021.1.00766
NGC 1052	0.48	54.0	1200	2016-05-26	CO(1-0)	794, 108	2015.1.00591
NGC 1052	0.03	26.2	600	2015-10-23	CO(2-1)	443, 223	2015.1.01290
NGC 1052	0.13	16.8	4300	2015-08-16	CO(3-2)	333, 344	2013.1.01225
NGC 1052	0.26	62.8	700	2017-07-28	HCN(1-0)	1020, 88	2016.1.00375
IC 4296	0.40	25	1700	2014-07-23	CO(2-1)	190, 226	2013.1.00229

Table 2. Details on the position and redshift of each source. All redshifts are barycentric and use the optical convention. RC3 is the Third Reference Catalogue of Bright Galaxies (de Vaucouleurs et al. 1991). Velocities are in km s^{-1}.

Source	RA, Dec. (J2000)	z_*	Redshift reference	v_*	$v_{mol} - v_*$
NGC 6868	20:09:54.1, −48:22:46.3	0.0095±0.0001 (FORS)	Rose et al. (2019b)	2830±30	−60±30
Abell S555	05:57:12.5, −37:28:36.5	0.0446±0.0001 (MUSE)	Rose et al. (2019b)	13364±30	−190±40
Hydra-A	09:18:05.7, −12:05:44.0	0.0544±0.0001 (MUSE)	Rose et al. (2019b)	16294±30	120±50
Abell 2390	21:53:36.8, +17:41:43.7	0.2304±0.0001 (VIMOS)	Hamer et al. (2016)	69074±30	170±40
RXCJ0439.0+0520	04:39:02.3, +05:20:43.7	0.2076±0.0001 (VIMOS)	Hamer et al. (2016)	62237±30	210±60
Abell 1644	12:57:11.6, −17:24:34.1	0.0473±0.0001 (MUSE)	Rose et al. (2019b)	14191±30	−60±40
Circinus	14:13:09.9, −65:20:21.0	0.00145±0.00001 (NED)	Ursini et al. (2023)	434 ± 3	–
IC 4296	13:36:39.1, −33:57:57.3	0.01247±0.00003 (NED)	Ruffa et al. (2019)	3738±10	−60±50
Abell 2597	23:25:19.7, −12:07:27.7	0.0821±0.0001 (MUSE)	Tremblay et al. (2018)	24613±30	20±40
NGC 5044	13:15:24.0, −16:23:07.6	0.0092±0.0001 (MUSE)	Rose et al. (2019b)	2761±30	30±40
NGC 1052	02:41:04.8, −08:15:20.8	0.00498±0.00002 (RC3)	de Vaucouleurs et al. (1991)	1492 ± 5	–
NGC 4261	12:19:23.2, +05:49:29.7	0.0073±0.0001 (OHP)	Matsumoto et al. (2001)	2200±30	−10±40
Centaurus-A	13:25:27.6, −43:01:09.0	0.00183 ± 0.00002 (NED)	Crook et al. (2007)	547±5	–

these maps have sometimes been made using a slightly smoothed image. This smoothing is typically done using a Gaussian kernel with dimensions equal to the image's beam. The impact this has on the effective image resolution is shown in the figure captions, and is also indicated by the beam size on each image. This smoothing means we can capture the velocity and velocity dispersion of more extended emission.

2.3 Moments maps and spectra

In Figs 1–12, we show intensity, velocity, and velocity dispersion maps made with each galaxy's molecular emission. We indicate the location of each galaxy's compact and unresolved radio continuum source with a cross, against which we extract the spectra of CO(1-0), CO(2-1), CN(2-1), HCO^+(2-1), and HCN(2-1). Typically, the ALMA observations span velocities from around −1500 to

Table 3. The classification of each galaxy and a brief summary of the molecular emission properties, including masses estimated in Section 3.3. Inclinations are taken from the HyperLeda data base – these sometimes differ from estimates of the inclination of the CO disc. For sources whose morphology and velocity distribution indicate a molecular disc, we estimate that disc's inclination using $\cos i = \sqrt{[(b/a)^2 - r_0^2]/[1 - r_0^2]}$, where a is the semimajor axis length, b the semiminor axis length, and r_0 is the disc thickness (Tully et al. 1998). We also assume circular disc and $r_0^2 = 0.2$, as suggested by Tully et al. (1998). As described in Section 3.3, molecular masses are estimated using a flux density ratio of $F_{ul} = 3.2$, but values as low as 2.14 have been reported (see Ruffa et al. 2022). As well as the quoted errors, which are estimated from noise in the spectra, this will introduce an additional systematic uncertainty.

Source	Galaxy type	Inclination/°	Molecular morphology	Molecular mass/$M_\odot$
NGC 6868	Elliptical	41	0.5 kpc wide disc inclined at ≈ 70°	$1.3\pm0.2 \times 10^8$
Abell S555	Unknown	–	Plume of 2.5 kpc as measured along l.o.s.	$5.6\pm0.5 \times 10^8$
Hydra-A	Elliptical-S0	79	5 kpc molecular disc inclined at ≈ 90°	$3.1\pm0.2 \times 10^9$
Abell 2390	Irregular	–	Plume of 15 kpc as measured along l.o.s.	$2.2\pm0.2 \times 10^{10}$
RXCJ0439.0+0520	Irregular	–	Plume of 9 kpc as measured along l.o.s.	$1.3\pm0.4 \times 10^{10}$
Abell 1644	Irregular	–	Clumps distributed along an arc	$1.6\pm0.3 \times 10^9$
Circinus	Sb spiral	64	Spiral arms inclined at ≈ 65° (Izumi et al. 2018)	–
IC 4296	Elliptical	90	0.5 kpc wide disc inclined at ≈ 68° (Ruffa et al. 2019)	$2.3\pm0.2 \times 10^7$
Abell 2597	Elliptical	68	Irregular central 7 kpc, faint emission to 30 kpc	$4.6\pm0.5 \times 10^9$
NGC 5044	Elliptical	43	One or two weak clumps 200–500 pc from the AGN, plus further clumps out to 6 kpc	$2.4\pm0.4 \times 10^{7a}$
NGC 1052	Elliptical	70	Gas poor with $5.3 \times 10^5 M_\odot$ CND (Kameno et al. 2020)	–
NGC 4261	Elliptical	56	200 pc wide disc inclined at ≈ 61° (Boizelle et al. 2021)	$2.1\pm0.2 \times 10^7$
Centaurus-A	S0	45	Dense gas along dust lane (Wild, Eckart & Wiklind 1997)	$1.4 \pm 0.2 \times 10^{9b}$

Note. [a]The molecular mass quoted for NGC 5044 is from the central 0.7 kpc. Within 6 kpc, a mass of 5.1×10^7 $M_\odot$ is found by David et al. (2014). [b]The molecular mass of Centaurus-A is taken from Parkin et al. (2012).

$+1500\,\mathrm{km\,s^{-1}}$, though we see no absorption or emission features outside the ranges shown in the spectra. On each spectrum, a red line shows the best fit. Where the absorption overlaps with emission, the emission has been subtracted and is shown by a dashed yellow line.

Sometimes, absorption from other lines is also present. Abell 1644 has CS(5-4) absorption. Hydra-A has several more molecules detected in absorption than we show, including HCO^+(1-0) HCN(1-0), H_2C(3-2), and ^{13}CO(2-1). These can be seen in Rose et al. (2020), along with the best fits. NGC 1052 has several more lines shown by Kameno et al. (2020). Finally, NGC 6868, Abell 2597, Abell 2390, Hydra-A, and NGC 4261 have H I absorption. We clearly distinguish these H I spectra by showing them in green. In Fig. 13, we also show HCO^+(2-1) and HCN(2-1) spectra seen against the central radio source of the iconic radio galaxy Centaurus-A, from Wiklind & Combes (1997a).

2.4 Line fitting

To determine the optimal fit for each spectrum, we first identify the minimum number of components required by incrementally adding Gaussian lines. We do this until no channel contains $> 5\sigma$ emission and the root mean square (RMS) value of the fitting region is less than 1.5 times that of the remainder of the spectrum. This threshold provides a good fit while not introducing unnecessary or unwarranted complexity.

We then perform an initial fit using `Python`'s `SciPy` library. Specifically, we use the `curve fit` minimization algorithm. Our fitting procedure is similar for both emission and absorption lines. However, when a spectrum contains overlapping emission and absorption features, the absorption must be masked while we first fit to the emission. This fit to the emission is then subtracted from the spectrum before fitting to the absorption. We do this masking by eye, which we find to be effective. Additionally, we find that using a reasonable range of masking boundaries results in minimal changes to the ultimate fits.

After making a best fit to a spectrum, we find the noise level. We take this to be the RMS of the continuum emission, excluding regions exhibiting emission or absorption features. Then, 10 000 simulated spectra are generated based upon the observed spectrum and the initial best fit. At each velocity channel, a pseudo random value is drawn from a Gaussian distribution centred at 0 and with a dispersion equal to the RMS noise. This value, which may be positive or negative, is then added to the original spectrum's best-fitting value for that velocity channel.

After repeating this for all velocity channels, a new simulated spectrum is produced. For each simulated spectrum, we then find a best fit in the same way as for the original spectrum. The 1σ upper and lower error bounds are then defined by the values that delineate the 15.865 per cent highest and lowest results among the 10 000 fits. This ensures that 68.27 per cent of the fitted parameters fall within the 1σ range.

Where the emission and absorption overlap, we do not account for errors from fitting to the emission propagating through to the absorption fits. This is because the former are generally much smaller.

The best-fitting parameters for each spectrum are shown in Table 4. The noise and channel width of each spectrum is shown in Table 5.

3 MOLECULAR GAS PROPERTIES

3.1 Excitation temperatures

The excitation temperature, $T_{\rm ex}$, of a two-level system is defined in terms of the number of particles in the upper state, $n_{\rm u}$ and lower state, n_l:

$$\frac{n_{\rm u}}{n_{\rm l}} = \frac{g_{\rm u}}{g_{\rm l}} \exp\left(-\frac{h\nu}{kT_{\rm ex}}\right), \quad (1)$$

where g is the statistical weight of each state. The excitation temperature should not be confused with the more familiar thermal temperature. Rather, it is the temperature that would be expected to produce the ratio of particles in the different energy levels when local thermodynamic equilibrium applies.

For optically thin gas in local thermodynamic equilibrium, the CO(1-0) and CO(2-1) velocity-integrated optical depths are related

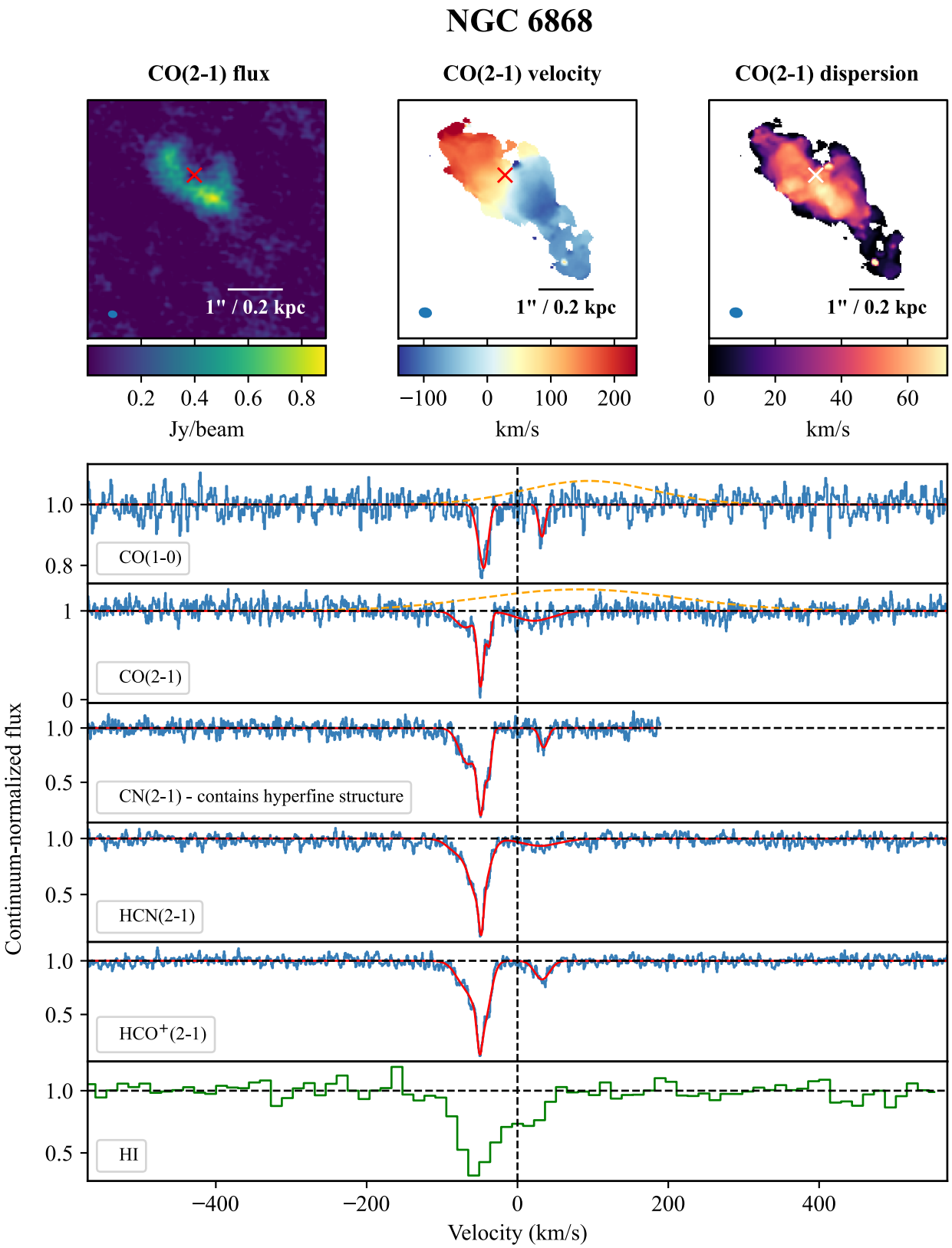

Figure 1. Intensity, velocity, and velocity dispersion maps of NGC 6868 made from CO(2-1) emission. The crosses indicate the location of the radio continuum source, against which the spectra of several different molecular lines are extracted and shown below. An H I spectrum also extracted against the radio core is shown in green (Tom Oosterloo, private communication). The dashed yellow lines show CO emission subtracted from the spectra. The flux map has a beam size of 0.17 × 0.14 arcsec. For the velocity and velocity dispersion maps, the smoothing applied increases the size to 0.24 × 0.19 arcsec.

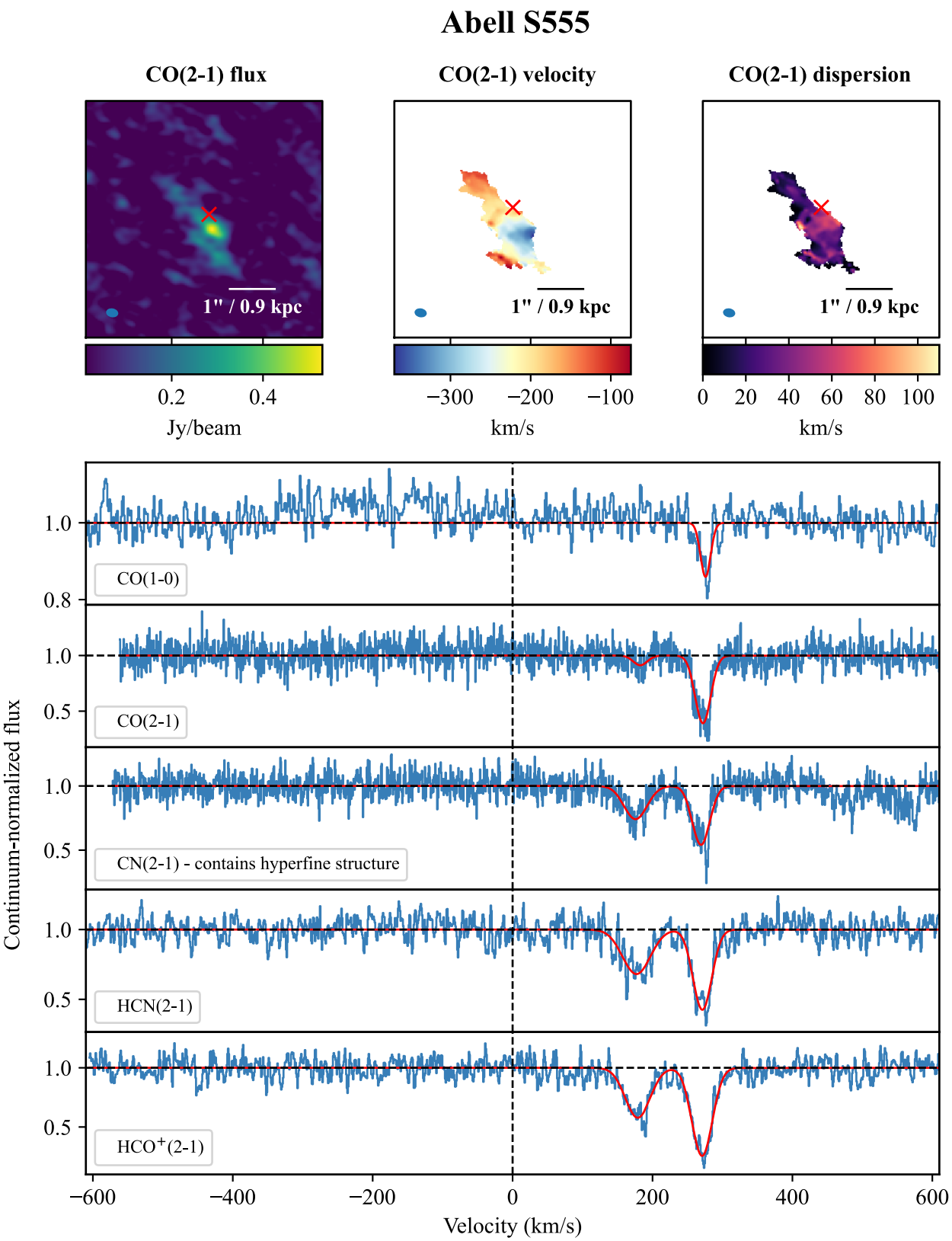

Figure 2. Intensity, velocity, and velocity dispersion maps of Abell S555 made from CO(2-1) emission. The crosses indicate the location of the radio continuum source, against which the spectra of several different molecular lines are extracted and shown below. The CO(1-0) observation has a larger beam size than the other observations, so its spectrum contains some of the more extended emission. The moments maps have a beam size of 0.26 × 0.19 arcsec.

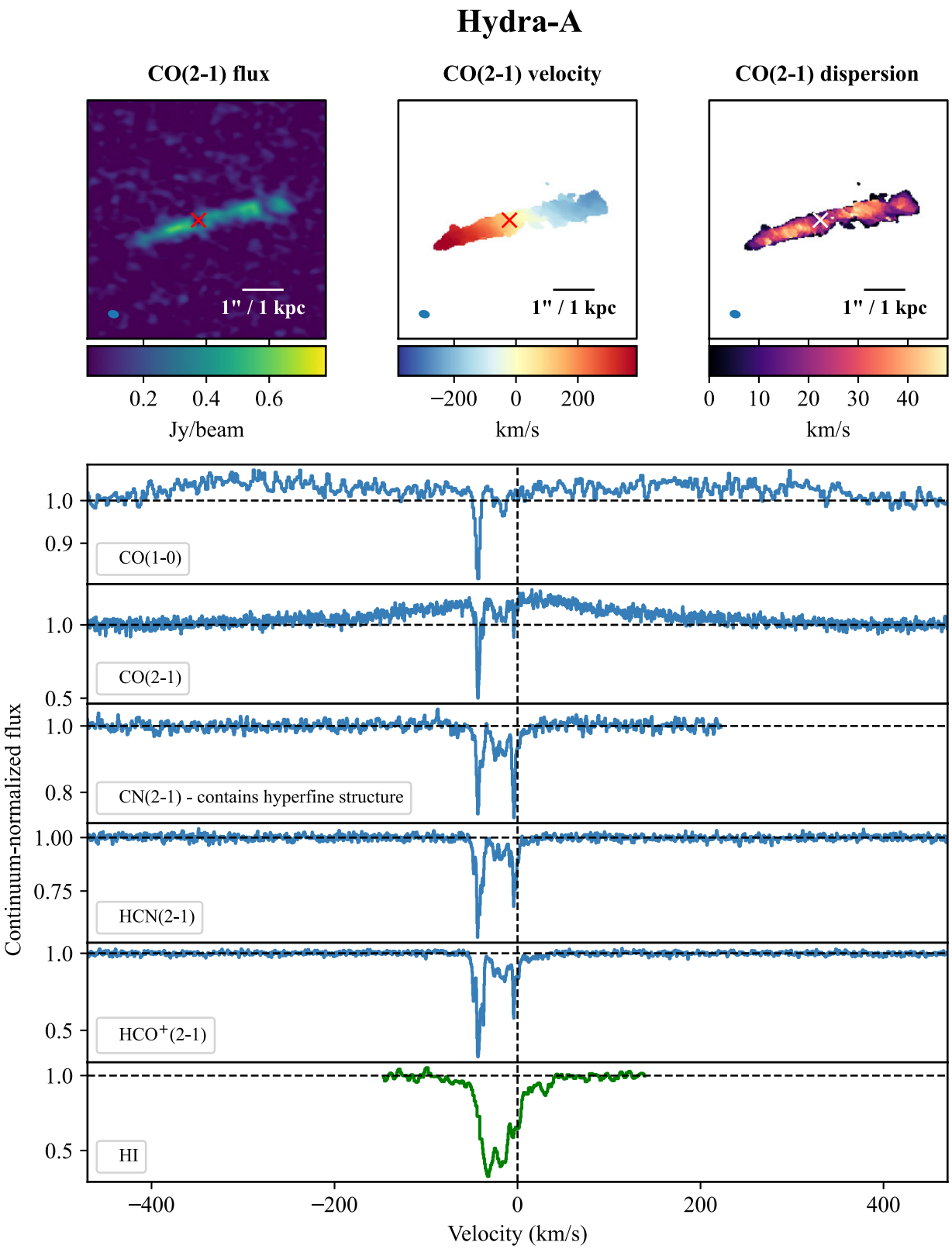

Figure 3. Intensity, velocity, and velocity dispersion maps of Hydra-A made from CO(2-1) emission. The crosses indicate the location of the radio continuum source, against which the spectra of several different molecular lines are extracted and shown below. An H I spectrum also extracted against the radio core is shown in green (Taylor 1996). Several more molecules are detected in absorption than presented here, including HCO^+(1-0) HCN(1-0), H_2C(3-2), and ^{13}CO(2-1). Spectra of these lines are shown in (Rose et al. 2020). Due to the complex nature of the absorption, we do not show best fits in the spectra above, but they can also be seen in (Rose et al. 2020). The moments maps have a beam size of 0.27 × 0.20 arcsec.

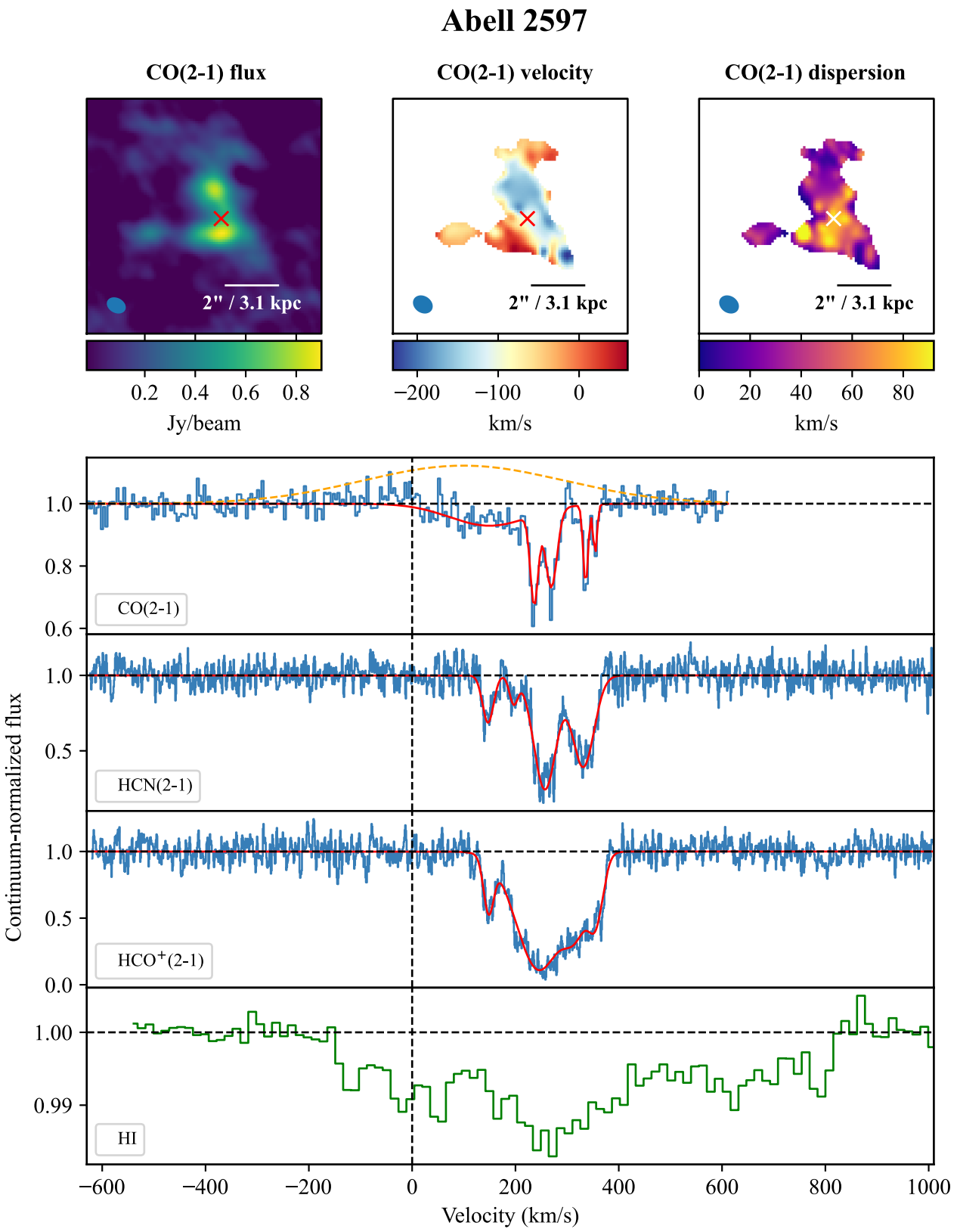

Figure 4. Intensity, velocity, and velocity dispersion maps of Abell 2597 made from CO(2-1) emission. The crosses indicate the location of the radio continuum source, against which the spectra of several different molecular lines are extracted and shown below. An H I spectrum also extracted against the radio core is shown in green (Hernández et al. 2008). The dashed yellow line shows subtracted CO emission. The moments maps have a beam size of 0.77 × 0.62 arcsec.

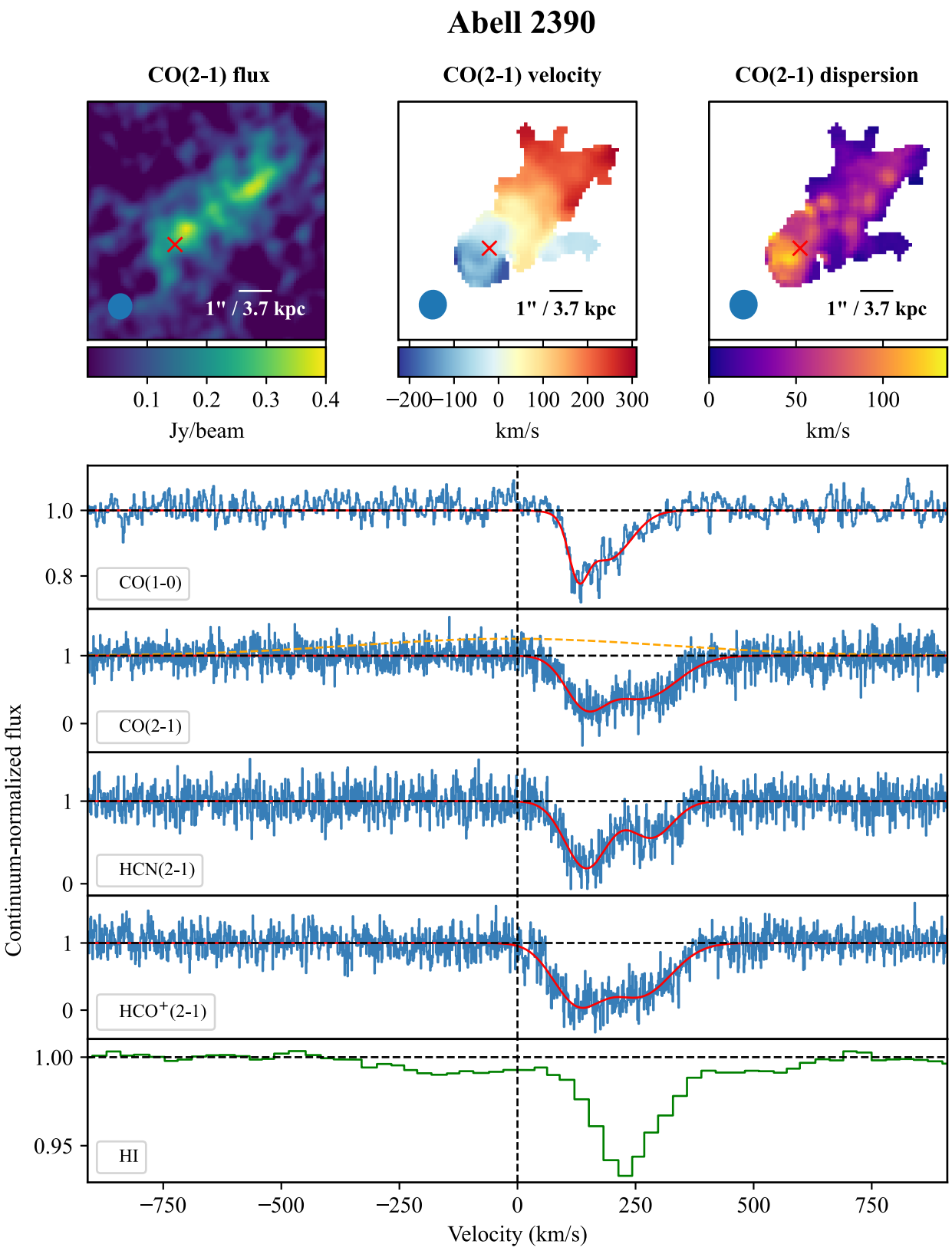

Figure 5. Intensity, velocity, and velocity dispersion maps of Abell 2390 made from CO(2-1) emission. The crosses indicate the location of the radio continuum source, against which the spectra of several different molecular lines are extracted and shown below. An H I spectrum also extracted against the radio core is shown in green (Hernández et al. 2008). The dashed yellow line shows subtracted CO emission. The flux map has a beam size of 0.80 × 0.73 arcsec. For the velocity and velocity dispersion maps, the smoothing applied increases the size to 0.90 × 0.85 arcsec.

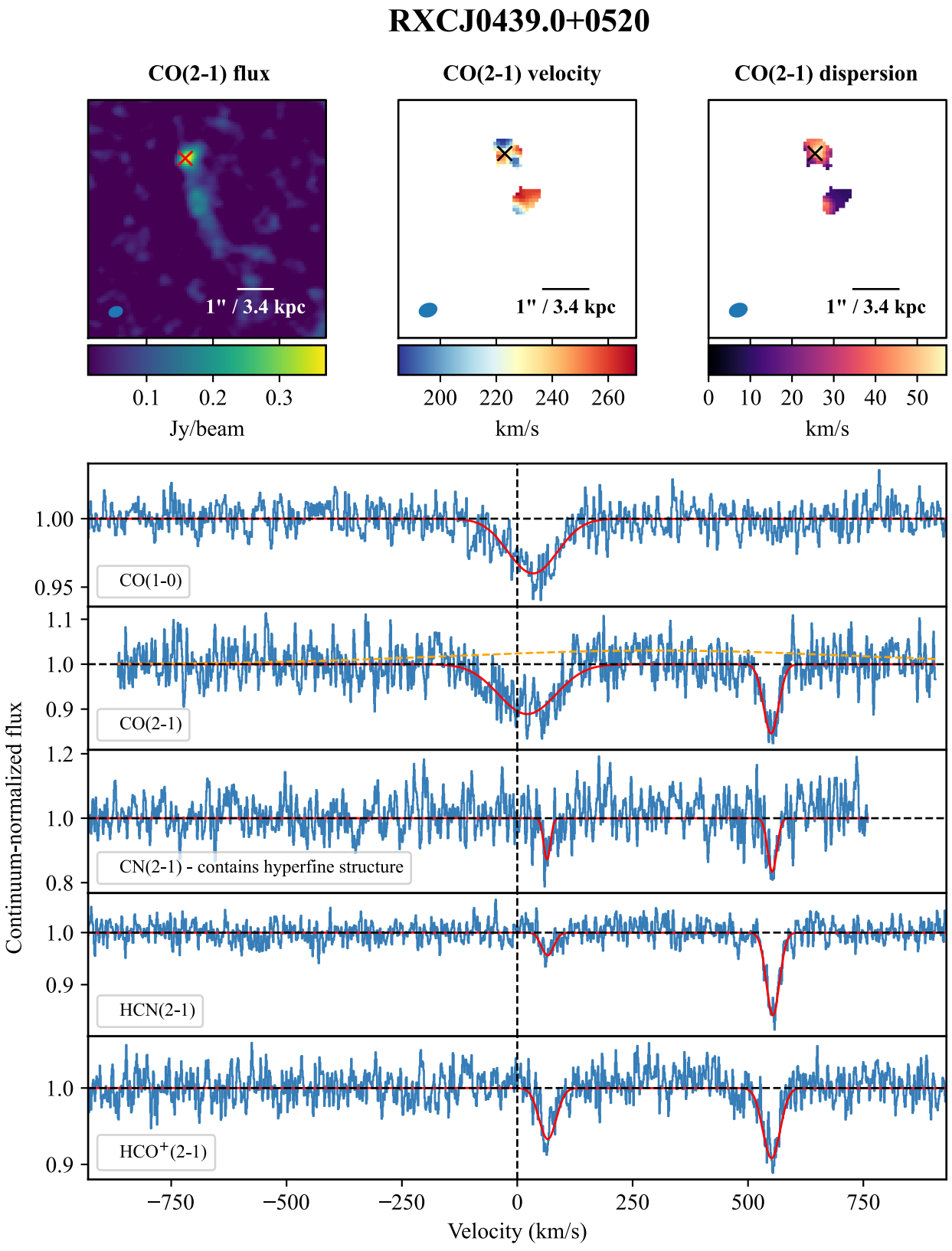

Figure 6. Intensity, velocity, and velocity dispersion maps of RXCJ0439.0+0520 made from CO(2-1) emission. The crosses indicate the location of the radio continuum source, against which the spectra of several different molecular lines are extracted and shown below. The dashed yellow line shows subtracted CO emission. The moments maps have a beam size of 0.41 × 0.30 arcsec. Note that a slightly smaller field of view is shown in the velocity and velocity dispersion maps.

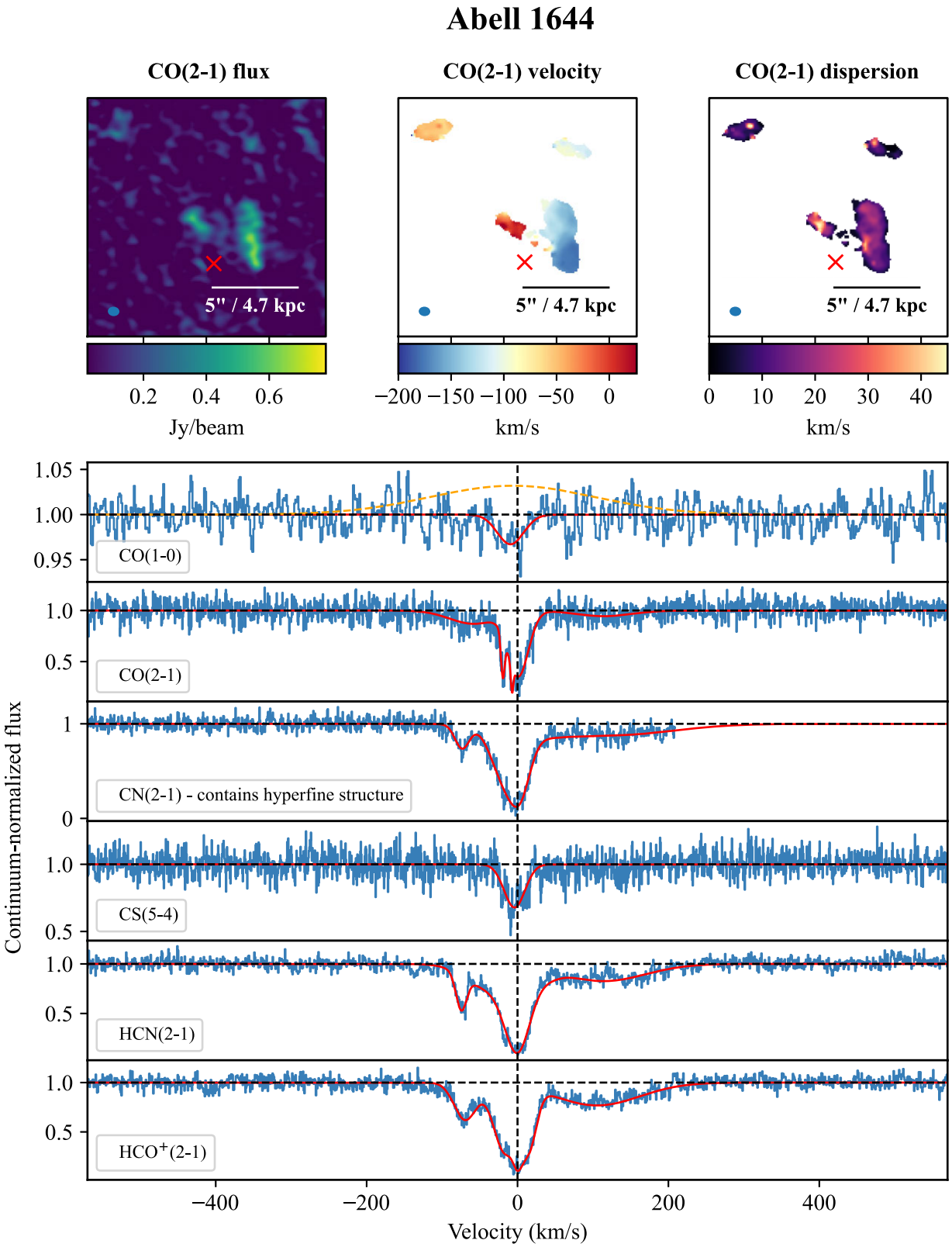

Figure 7. Intensity, velocity, and velocity dispersion maps of Abell 1644 made from CO(2-1) emission. The crosses indicate the location of the radio continuum source, against which the spectra of several different molecular lines are extracted and shown below. The dashed yellow line shows subtracted CO emission. Note that the angular resolution of the CO(1-0) observation is much larger than in CO(2-1) – 1.74 arcsec versus 0.47 arcsec. The emission subtracted from the CO(1-0) spectrum is therefore from the more extended structures visible in the CO(2-1) map, and not from closer to the radio core. The moments maps have a beam size of 0.67 × 0.54 arcsec.

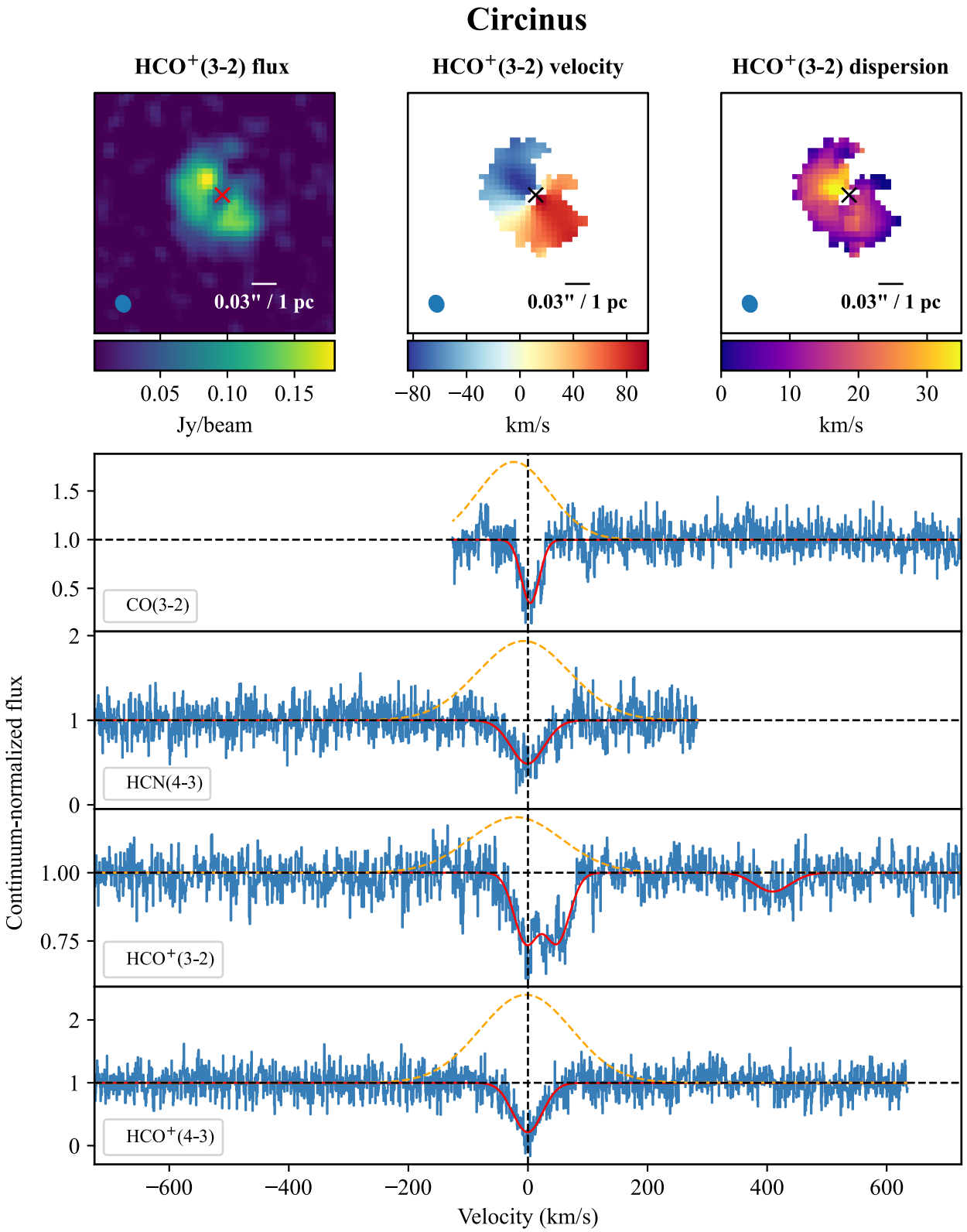

Figure 8. Intensity, velocity, and velocity dispersion maps of Circinus made from HCO^+(3-2) emission. The crosses indicate the location of the radio continuum source, against which the spectra of several different molecular lines are extracted and shown below. The dashed yellow lines show the emission subtracted from each spectrum. The moments maps have a beam size of 0.022 × 0.019 arcsec.

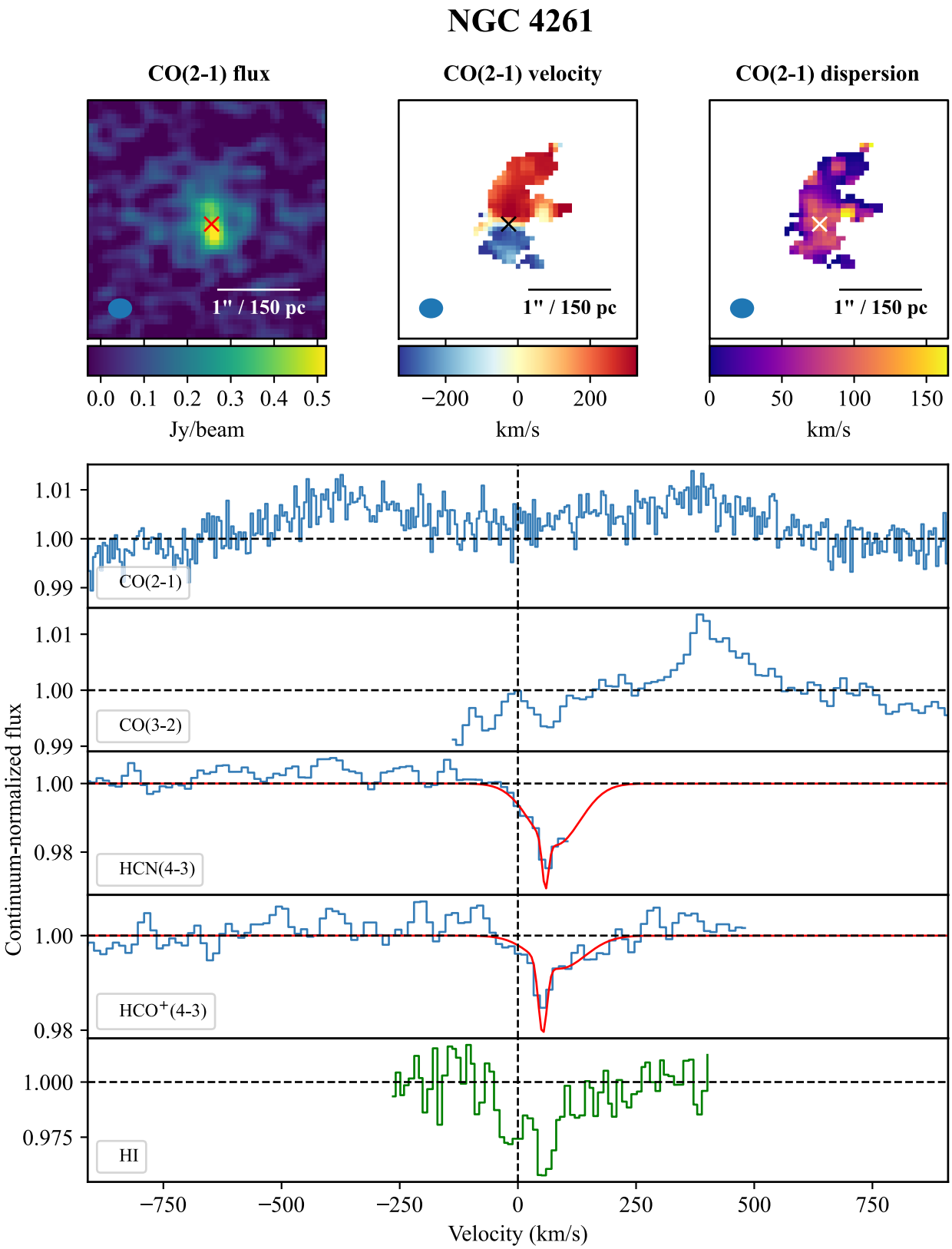

Figure 9. Intensity, velocity, and velocity dispersion maps of NGC 4261 made from CO(2-1) emission. The crosses indicate the location of the radio continuum source, against which the spectra of different molecular lines are extracted and shown below. The HCN(4-3) and HCO^+(4-3) lines are serendipitous detections found in archival data and unfortunately are close to the edge of the spectral range. An H I spectrum also extracted against the radio core is shown in green (Jaffe & McNamara 1994). The moments maps all have a beam size of 0.29 × 0.24 arcsec.

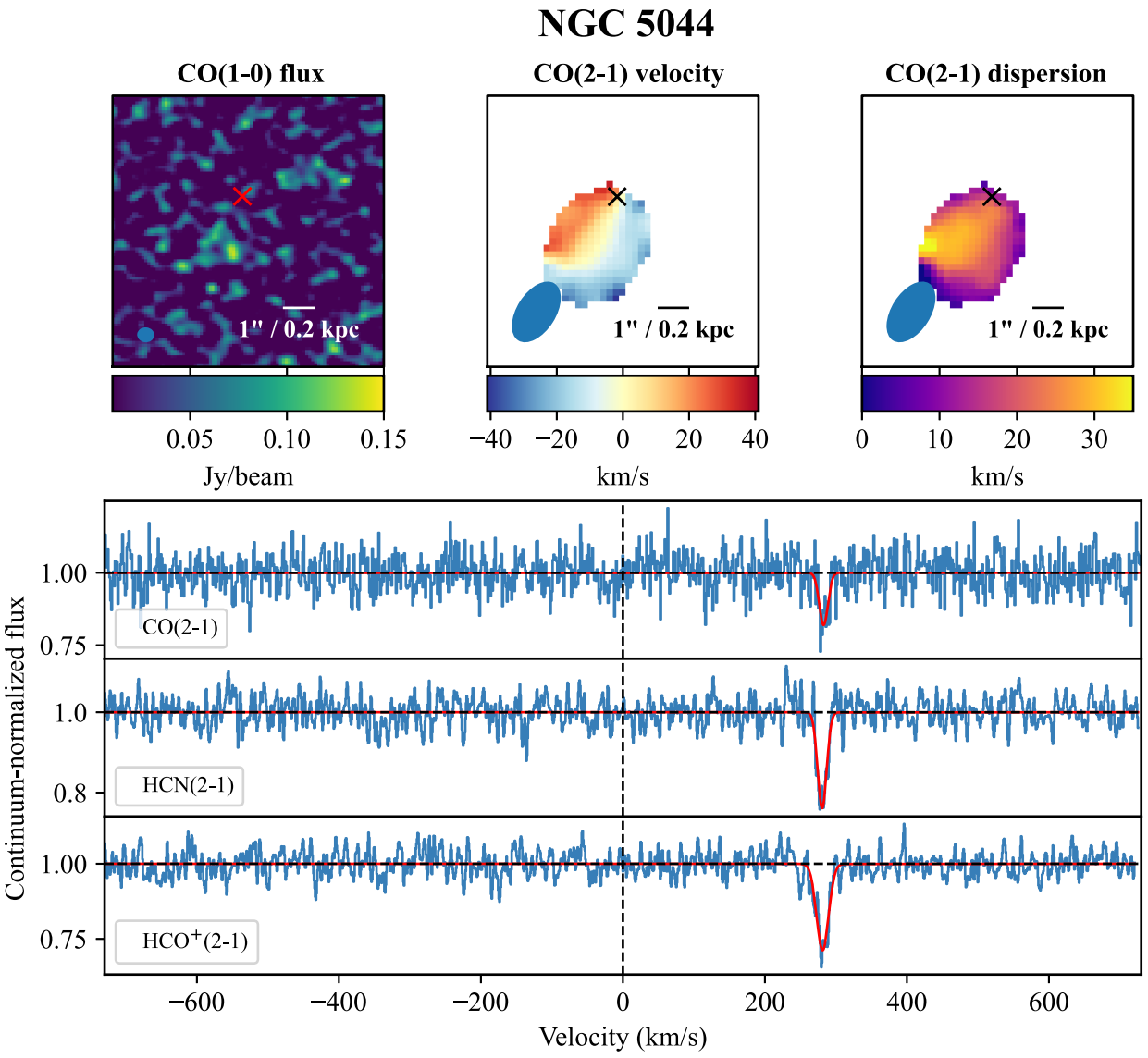

Figure 10. Intensity, velocity, and velocity dispersion maps of NGC 5044 made from CO(1-0) and CO(2-1) emission. The crosses indicate the location of the radio continuum source, against which we extract spectra of three molecular lines. The CO(1-0) flux map has a beam size of 0.54 × 0.47 arcsec. For the CO(2-1) velocity and velocity dispersion maps, the beam size is 2.2 × 1.2 arcsec.

by

$$\frac{\int \tau_{21} \mathrm{d}v}{\int \tau_{10} \mathrm{d}v} = 2 \frac{1 - \mathrm{e}^{-h\nu_{21}/kT_{\mathrm{ex}}}}{\mathrm{e}^{h\nu_{10}/kT_{\mathrm{ex}}} - 1} \quad , \tag{2}$$

where h and k are the Planck and Boltzmann constants, ν_{10} and ν_{21} are the rest frequencies of the CO(1-0) and CO(2-1) lines, and T_{ex} is the excitation temperature (Bolatto et al. 2003; Godard et al. 2010; Mangum & Shirley 2015). According to equation (2), the ratio of CO(2-1)/CO(1-0) velocity-integrated optical depths can be in the range of 0 to 4. These, respectively, correspond to the extreme cases where $k\mathrm{T_{ex}} << \mathrm{h}\nu$ and $k\mathrm{T_{ex}} >> \mathrm{h}\nu$.

For each galaxy where we have CO(1-0) and CO(2-1) absorption, we estimate the ratios of the velocity-integrated optical depths and the implied excitation temperatures. These are shown in Table 6. We generally estimate a single excitation temperature for each system's absorption, even though in many cases separate components are clearly present. This is because these components overlap significantly and are heavily degenerate. RXCJ0439.0+0520 is the exception, where the two components of absorption are separated by 500 km s^{-1}. We therefore calculate two excitation temperatures.

Many of the CO(2-1)/CO(1-0) ratios in Table 6 fall outside the feasible range of 0–4 and therefore give a negative excitation temperature. The excitation temperature may be negative when $n_{\mathrm{u}}/g_{\mathrm{u}} > n_{\mathrm{l}}/g_{\mathrm{l}}$, which is possible if there is pumping by a maser (Lo 2005). However, this effect is not possible in CO. Therefore, one or more of the assumptions made in our calculations is incorrect.

One possibility is that the gas is not in local thermodynamic equilibrium, i.e. the excitation temperature may vary between the different rotational levels. If the CO(1-0) excitation temperature is 20 K and the CO(2-1) excitation temperature is 5 K, then a ratio in the velocity-integrated optical depths of 5.6 is expected. This temperature difference is at the more extreme end of what could be expected, but is still far from explaining the ratios of over 10 which we see in the absorption lines of some systems.

A second assumption implicit in our calculations is that the size of the continuum source does not change between the frequencies of the

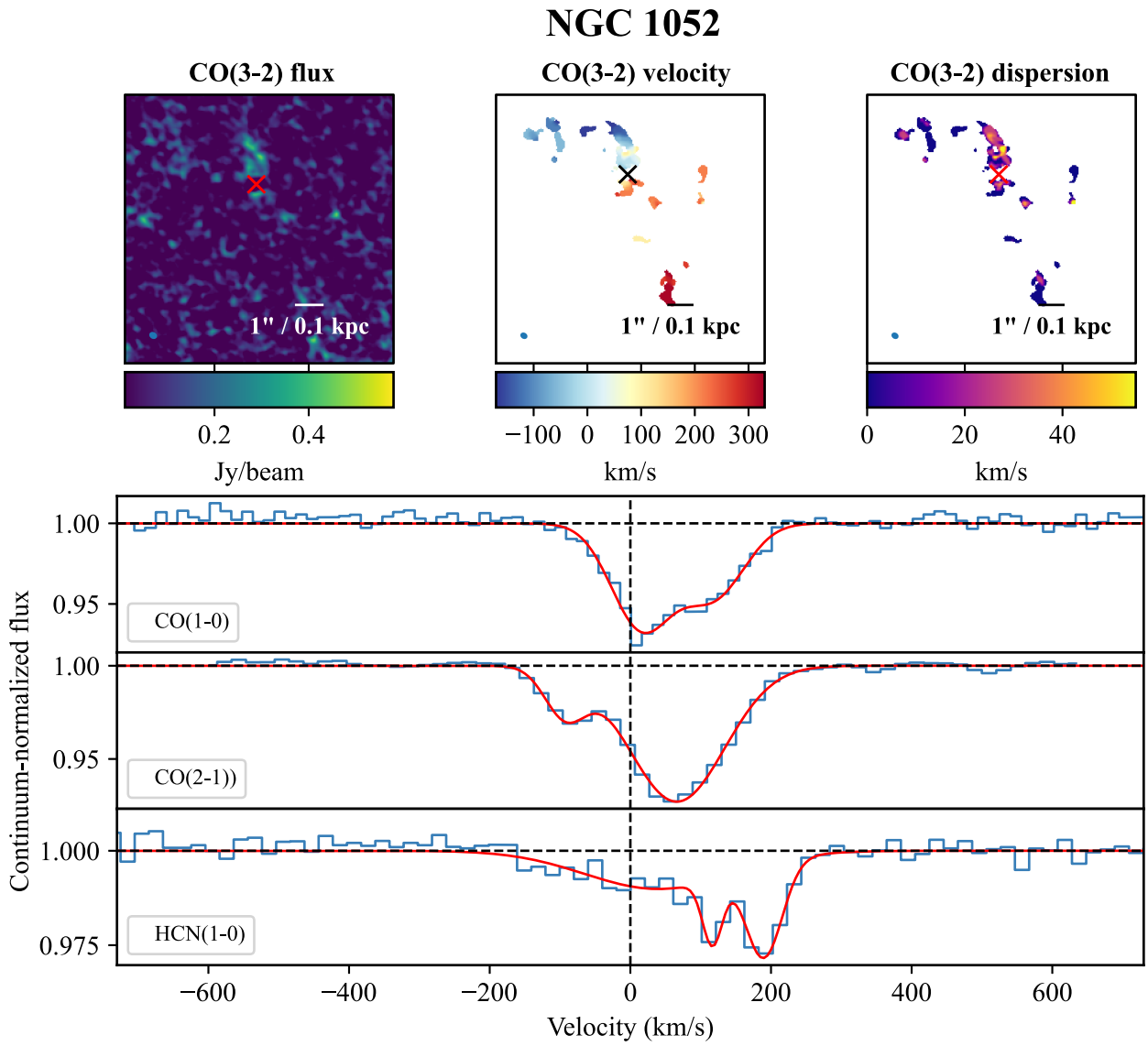

Figure 11. Intensity, velocity, and velocity dispersion maps of NGC 1052 made from CO(3-2) emission. The crosses indicate the location of the radio continuum source, against which the spectra of three different molecular lines are extracted and shown below. The moments maps have a beam size of 0.28 × 0.23 arcsec.

CO(1-0) and CO(2-1) lines. This can alter the line of sight at different frequencies, changing how the clouds intercept the continuum. We explore this possibility in more detail in our discussion. In the mean time however, we proceed to estimate molecular column densities assuming the ground state excitation temperature of the molecular gas is 5 K for all of the molecular lines.

3.2 Absorption column density estimates

The line-of-sight column density, $N_{\rm tot}$, of an optically thin molecular absorption region is

$$N_{\rm tot}^{\rm thin} = Q(T)\frac{8\pi\,\nu_{ul}^3}{c^3}\frac{g_l}{g_u}\frac{1}{A_{ul}}\frac{1}{1-{\rm e}^{-h\nu_{ul}/kT_{\rm ex}}}\int \tau_{ul}\,{\rm d}v\,, \tag{3}$$

where $Q(T)$ is the partition function, c is the speed of light, A_{ul} is the Einstein coefficient of the observed transition, and g the level degeneracy, with the subscripts u and l representing the upper and lower levels (Godard et al. 2010; Mangum & Shirley 2015).

The assumption of optically thin absorption in equation (3) is inappropriate for some of our data. To account for this, a correction factor from Mangum & Shirley (2015) can be applied to give the following more accurate column density:

$$N_{\rm tot} = N_{\rm tot}^{\rm thin}\frac{\tau}{1-\exp(-\tau)}. \tag{4}$$

This gives the column density of the absorbing molecule as a number density per square cm.

Table 7 shows the column densities estimated using the above equations, each object's molecular absorption lines and the best fits shown in Table 4. By far the most dominant error in our calculations of the column densities is the gas excitation temperature, $T_{\rm ex}$. We therefore use only the central estimate of the velocity-integrated optical depth in our calculations.

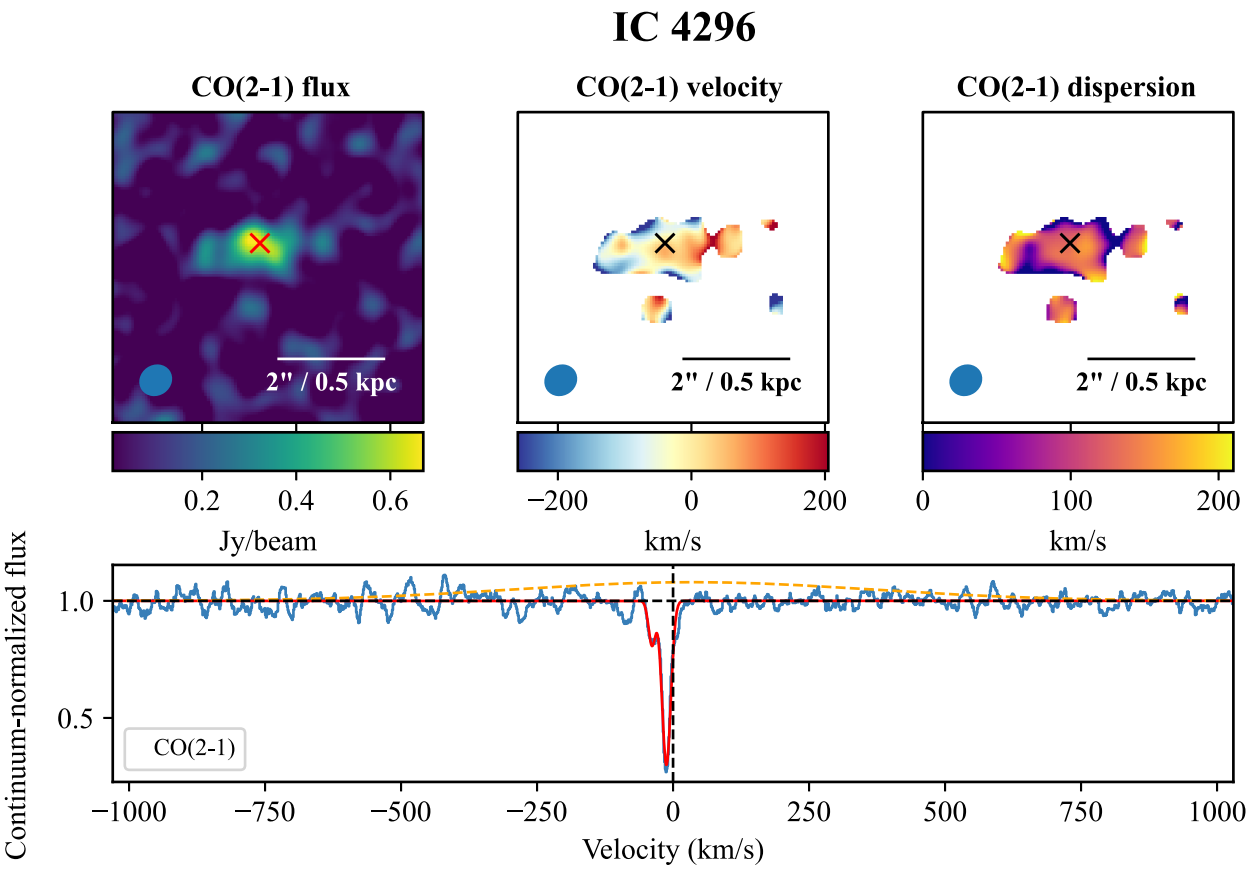

Figure 12. Intensity, velocity, and velocity dispersion maps of IC 4296 made from CO(2-1) emission. The crosses indicate the location of the radio continuum source, against which the spectrum of CO(2-1) is extracted and shown below. The dashed yellow line shows subtracted CO emission. The moments maps have a beam size of 0.63 × 0.57 arcsec.

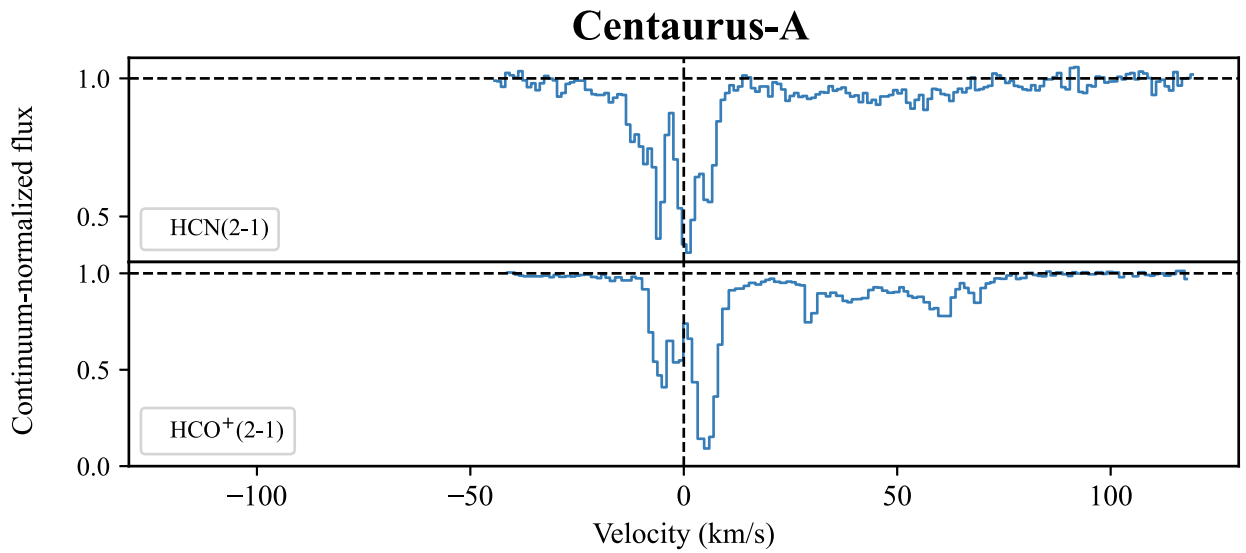

Figure 13. Spectra extracted from along the line of sight to the central radio continuum source of Centaurus-A, from Wiklind & Combes (1997a). Fits to the spectra can also be seen in that paper. Note that the velocity range of this spectrum is much narrower than in many of the preceding figures.

Table 4. The best-fitting parameters for the Gaussian fits made to each spectrum in Figs 1–12. Amplitudes are normalized to the continuum strength. Absorption lines have a negative amplitude and emission lines a positive amplitude. For Hydra-A, we refer readers to Rose et al. (2020).

Source	Line	A ($km\,s^{-1}$)	v_{cen}	σ ($km\,s^{-1}$)
NGC 6868	CO(1-0)	$0.075^{+0.011}_{-0.010}$	94^{+23}_{-25}	85^{+17}_{-15}
		$-0.21^{+0.02}_{-0.02}$	-45^{+1}_{-1}	$6.5^{+0.4}_{-0.4}$
		$-0.10^{+0.02}_{-0.02}$	33^{+1}_{-1}	$4.4^{+0.5}_{-0.4}$
	CO(2-1)	$0.24^{+0.02}_{-0.02}$	83^{+7}_{-7}	131^{+11}_{-10}
		$-0.19^{+0.02}_{-0.02}$	-68^{+3}_{3-}	13^{+3}_{-2}
		$-0.80^{+0.06}_{-0.04}$	-49^{+1}_{-1}	$3.9^{+0.4}_{-0.3}$
		$-0.37^{+0.03}_{-0.04}$	-38^{+1}_{-1}	$3.3^{+0.8}_{-0.4}$
		$-0.11^{+0.01}_{-0.01}$	22^{+3}_{-2}	24^{+3}_{-2}
	CN(2-1)	$-0.33^{+0.02}_{-0.02}$	-64^{+2}_{-2}	13^{+1}_{-1}
		$-0.63^{+0.05}_{-0.05}$	-48^{+1}_{-1}	$4.5^{+0.4}_{-0.4}$
		$-0.36^{+0.04}_{-0.04}$	-38^{+1}_{-1}	$3.3^{+0.5}_{-0.4}$
		$-0.18^{+0.02}_{-0.02}$	35^{+1}_{-1}	$5.4^{+0.7}_{-0.6}$
	HCN(2-1)	$-0.11^{+0.02}_{-0.02}$	-73^{+1}_{-1}	$4.5^{+2.0}_{-0.9}$
		$-0.41^{+0.03}_{-0.03}$	-57^{+3}_{-1}	15^{+2}_{-3}
		$-0.46^{+0.02}_{-0.02}$	-48^{+1}_{-1}	$4.6^{+0.3}_{-0.3}$
		$-0.083^{+0.01}_{-0.01}$	29^{+2}_{-2}	16^{+2}_{-2}
	HCO^+(2-1)	$-0.19^{+0.01}_{-0.01}$	-72^{+2}_{-1}	10^{+1}_{-1}
		$-0.72^{+0.03}_{-0.02}$	-48^{+1}_{-1}	$8.9^{+0.4}_{-0.4}$
		$-0.05^{+0.01}_{-0.01}$	-40^{+2}_{-2}	9.1^{+2}_{-2}
		$-0.17^{+0.01}_{-0.01}$	33^{+1}_{-1}	10^{+1}_{-1}
Abell S555	CO(1-0)	$0.05^{+0.01}_{-0.01}$	-186^{+11}_{-10}	260^{+20}_{-20}
		$-0.14^{+0.02}_{-0.02}$	276^{+1}_{-1}	$7.2^{+1.0}_{-0.9}$
	CO(2-1)	$-0.09^{+0.02}_{-0.02}$	182^{+3}_{-3}	10^{+4}_{-3}
		$-0.61^{+0.02}_{-0.02}$	272^{+1}_{-1}	11^{+1}_{-1}
	CN(2-1)	$-0.26^{+0.01}_{-0.02}$	176^{+1}_{-1}	16^{+1}_{-1}
		$-0.46^{+0.02}_{-0.02}$	269^{+1}_{-1}	13^{+1}_{-1}
	HCN(2-1)	$-0.32^{+0.01}_{-0.01}$	177^{+1}_{-1}	20^{+1}_{-1}
		$-0.58^{+0.02}_{-0.02}$	271^{+1}_{-1}	13^{+1}_{-1}
	HCO^+(2-1)	$-0.41^{+0.02}_{-0.02}$	179^{+1}_{-1}	18^{+1}_{-1}
		$-0.74^{+0.02}_{-0.02}$	271^{+1}_{-1}	15^{+1}_{-1}
Abell 2597	CO(2-1)	$0.12^{+0.01}_{-0.01}$	99^{+16}_{-14}	195^{+24}_{-32}
		$-0.07^{+0.01}_{-0.01}$	150^{+10}_{-9}	77^{+9}_{-8}
		$-0.29^{+0.02}_{-0.02}$	236^{+3}_{-2}	$7.6^{+0.7}_{-0.6}$
		$-0.25^{+0.02}_{-0.02}$	269^{+3}_{-2}	11^{+1}_{-1}
		$-0.26^{+0.03}_{-0.02}$	336^{+3}_{-2}	$4.7^{+0.6}_{-0.6}$
		$-0.16^{+0.03}_{-0.03}$	354^{+3}_{-2}	$3.9^{+1.0}_{-0.7}$
	HCN(2-1)	$-0.31^{+0.02}_{-0.02}$	147^{+1}_{-1}	11^{+1}_{-1}
		$-0.18^{+0.02}_{-0.02}$	197^{+1}_{-1}	8.3^{+1}_{-1}
		$-0.76^{+0.01}_{-0.01}$	257^{+2}_{-2}	22^{+1}_{-1}
		$-0.60^{+0.02}_{-0.02}$	331^{+2}_{-2}	21^{+1}_{-1}
	HCO^+(2-1)	$-0.40^{+0.02}_{-0.02}$	148^{+1}_{-1}	10^{+1}_{-1}
		$-0.89^{+0.02}_{-0.02}$	246^{+3}_{-3}	45^{+4}_{-3}
		$-0.43^{+0.05}_{-0.06}$	320^{+3}_{-3}	24^{+5}_{-4}
		$-0.41^{+0.06}_{-0.07}$	357^{+2}_{-3}	14^{+2}_{-2}
Abell 2390	CO(1-0)	$-0.15^{+0.02}_{-0.03}$	128^{+2}_{-2}	20^{+3}_{-3}
		$-0.015^{+0.02}_{-0.02}$	190^{+5}_{-4}	50^{+5}_{-4}
	CO(2-1)	$0.25^{+0.02}_{-0.02}$	-140^{+20}_{-20}	330^{+30}_{-30}
		$-0.74^{+0.04}_{-0.03}$	147^{+4}_{-4}	45^{+2}_{-2}
		$-0.62^{+0.02}_{-0.02}$	275^{+5}_{-5}	62^{+4}_{-4}
	HCN(2-1)	$-0.81^{+0.02}_{-0.02}$	145^{+2}_{-2}	45^{+2}_{-2}
		$-0.44^{+0.02}_{-0.02}$	283^{+4}_{-4}	45^{+4}_{-4}
	HCO^+(2-1)	$-0.86^{+0.05}_{-0.05}$	126^{+5}_{-5}	52^{+3}_{-3}
		$-0.78^{+0.03}_{-0.03}$	260^{+7}_{-7}	65^{+5}_{-5}
RXCJ0439.0+0520	CO(1-0)	$-0.040^{+0.002}_{-0.002}$	34^{+3}_{-3}	54^{+3}_{-3}
	CO(2-1)	$0.031^{+0.002}_{-0.002}$	300^{+80}_{-70}	430^{+120}_{-100}
		$-0.11^{+0.01}_{-0.01}$	22^{+3}_{-3}	62^{+3}_{-3}
		$-0.15^{+0.01}_{-0.01}$	550^{+1}_{-1}	16^{+1}_{-1}
	CN(2-1)	$-0.13^{+0.02}_{-0.02}$	64^{+1}_{-1}	7.4^{+1}_{-1}
		$-0.17^{+0.02}_{-0.02}$	553^{+1}_{-1}	9.8^{+1}_{-1}
	HCN(2-1)	$-0.04^{+0.01}_{-0.01}$	66^{+2}_{-2}	13^{+2}_{-2}
		$-0.16^{+0.01}_{-0.01}$	554^{+2}_{-2}	14^{+2}_{-2}
	HCO^+(2-1)	$-0.07^{+0.01}_{-0.01}$	66^{+1}_{-1}	18^{+1}_{-1}
		$-0.09^{+0.01}_{-0.01}$	551^{+1}_{-1}	19^{+1}_{-1}
Abell 1644	CO(1-0)	$0.032^{+0.002}_{-0.002}$	-6^{+12}_{-11}	110^{+}_{-}
		$-0.033^{+0.004}_{-0.004}$	-9^{+3}_{-3}	17^{+3}_{-2}
	CO(2-1)	$-0.13^{+0.01}_{-0.01}$	-58^{+5}_{-5}	32^{+3}_{-3}
		$-0.40^{+0.03}_{-0.03}$	-19^{+1}_{-1}	$2.4^{+0.3}_{-0.3}$
		$-0.25^{+0.03}_{-0.03}$	-7^{+2}_{-1}	$1.6^{+0.3}_{-0.2}$
		$-0.63^{+0.03}_{-0.03}$	1^{+2}_{-3}	14^{+2}_{-1}
		$-0.06^{+0.01}_{-0.01}$	115^{+5}_{-5}	37^{+5}_{-5}
	CN(2-1)	$-0.24^{+0.02}_{-0.02}$	-73^{+2}_{-2}	10^{+1}_{-1}
		$-0.81^{+0.05}_{-0.05}$	-6^{+3}_{-3}	21^{+3}_{-2}
		$-0.12^{+0.04}_{-0.04}$	110^{+7}_{-7}	98^{+12}_{-11}
	CS(5-4)	$-0.32^{+0.01}_{-0.01}$	-4^{+1}_{-1}	14^{+1}_{-1}
	HCN(2-1)	$-0.36^{+0.03}_{-0.03}$	-74^{+3}_{-3}	7.0^{+4}_{-3}
		$-0.27^{+0.04}_{-0.05}$	-31^{+4}_{-4}	32^{+5}_{-4}
		$-0.26^{+0.05}_{-0.05}$	-17^{+3}_{-3}	3^{+3}_{-1}
		$-0.62^{+0.06}_{-0.06}$	2^{+2}_{-2}	16^{+4}_{-3}
		$-0.18^{+0.01}_{-0.01}$	111^{+5}_{-6}	58^{+6}_{-6}
	HCO^+(2-1)	$-0.38^{+0.01}_{-0.01}$	-69^{+1}_{-1}	15^{+1}_{-1}
		$-0.68^{+0.05}_{-0.04}$	-18^{+3}_{-3}	14^{+2}_{-2}
		$-0.35^{+0.05}_{-0.05}$	0^{+2}_{-2}	7^{+3}_{-2}
		$-0.53^{+0.06}_{-0.06}$	15^{+4}_{-3}	10^{+2}_{-2}
		$-0.23^{+0.01}_{-0.01}$	105^{+2}_{-2}	56^{+4}_{-3}
Circinus	CO(3-2)	$0.80^{+0.03}_{-0.03}$	-16^{+3}_{-3}	60^{+3}_{-3}
		$-0.65^{+0.03}_{-0.03}$	12^{+1}_{-1}	15^{+2}_{-1}
	HCN(4-3)	$0.97^{+0.02}_{-0.02}$	1^{+2}_{-2}	77^{+2}_{-2}
		$-0.51^{+0.03}_{-0.03}$	7^{+2}_{-2}	28^{+2}_{-2}
	HCO^+(3-2)	$0.25^{+0.02}_{-0.01}$	-12^{+4}_{-4}	77^{+14}_{-12}
		$-0.25^{+0.01}_{-0.01}$	-1^{+3}_{-3}	20^{+2}_{-1}
		$-0.26^{+0.01}_{-0.01}$	55^{+3}_{-3}	21^{+2}_{-2}
		$-0.07^{+0.01}_{-0.01}$	417^{+4}_{-4}	29^{+5}_{-5}
	HCO^+(4-3)	$1.40^{+0.02}_{-0.02}$	-5^{+2}_{-2}	77^{+2}_{-1}
		$-0.79^{+0.03}_{-0.03}$	8^{+1}_{-1}	25^{+1}_{-1}
NGC 4261	HCN(4-3)	$-0.015^{+0.005}_{-0.005}$	82^{+2}_{-1}	$5.9^{+3.7}_{-2.2}$
		$-0.018^{+0.002}_{-0.002}$	104^{+14}_{-7}	54^{+11}_{-7}
	HCO^+(4-3)	$-0.015^{+0.012+}_{-0.006-}$	76^{+8}_{-6}	8^{+5}_{-3}
		$-0.007^{+0.003}_{-0.002}$	108^{+20}_{-20}	58^{+17}_{-16}

Table 4 – *continued*

Source	Line	A ($km\,s^{-1}$)	v_{cen}	σ ($km\,s^{-1}$)
NGC 5044	CO(2-1)	$-0.18^{+0.03}_{-0.03}$	283^{+1}_{-1}	$6.0^{+1.3}_{-1.1}$
	HCN(2-1)	$-0.24^{+0.01}_{-0.01}$	281^{+1}_{-1}	$6.3^{+0.7}_{-0.6}$
	HCO^+(2-1)	$-0.29^{+0.01}_{-0.01}$	281^{+1}_{-1}	$8.4^{+0.6}_{-0.5}$
NGC 1052	CO(1-0)	$-0.066^{+0.011}_{-0.010}$	18^{+17}_{-17}	43^{+9}_{-8}
		$-0.049^{+0.012}_{-0.012}$	121^{+20}_{-31}	39^{+11}_{-9}
	CO(2-1)	$-0.027^{+0.04}_{-0.04}$	-93^{+7}_{-7}	29^{+7}_{-6}
		$-0.073^{+0.03}_{-0.03}$	66^{+4}_{-4}	68^{+4}_{-4}
	HCN(1-0)	$-0.010^{+0.001}_{-0.001}$	33^{+20}_{-18}	100^{+20}_{-13}
		$-0.018^{+0.002}_{-0.002}$	117^{+4}_{-3}	15^{+6}_{-2}
		$-0.025^{+0.002}_{-0.002}$	190^{+3}_{-2}	25^{+5}_{-3}
IC 4296	CO(2-1)	$-0.19^{+0.01}_{-0.02}$	-39^{+1}_{-1}	$6.3^{+0.7}_{-0.6}$
		$-0.70^{+0.01}_{-0.01}$	-12^{+1}_{-1}	$8.1^{+0.3}_{-0.2}$

3.3 Molecular mass estimates

The molecular mass associated with CO emission can be estimated using the following relation from Bolatto, Wolfire & Leroy (2013):

$$M_{mol} = \frac{1.05\times10^4}{F_{ul}}\left(\frac{X_{CO}}{2\times10^{20}\,\frac{cm^{-2}}{K\,km\,s^{-1}}}\right)\left(\frac{1}{1+z}\right) \times \left(\frac{S_{CO}\Delta v}{Jy\,km\,s^{-1}}\right)\left(\frac{D_L}{Mpc}\right)^2 M_\odot, \quad (5)$$

where M_{mol} is the mass of molecular hydrogen, X_{CO} is a CO-to-H_2 conversion factor, z is the source's redshift, $S_{CO}\Delta v$ is the emission integral, and D_L is the luminosity distance in Mpc. F_{ul} is an approximate conversion factor for the expected flux density ratios of the CO(1-0) and CO(2-1) lines, where u and l represent the upper and lower levels. For CO(1-0), $F_{10} = 1$ and for CO(2-1), we adopt a value of $F_{21} = 3.2$ from Braine & Combes (1992), which has been used by similar studies (e.g. David et al. 2014; Tremblay et al. 2016; Rose et al. 2019b). However, F_{ul} is a major source of uncertainty, with lower values of 2.32 reported by Ocaña Flaquer et al. (2010) and Ruffa et al. (2019) and a value of 2.14 by Ruffa et al. (2022).

To ensure our mass estimates are comparable with similar studies, we use the standard Milky Way CO-to-H_2 conversion factor of $X_{CO} = 2\times10^{20}$ cm^{-2} $(K\,km\,s^{-1})^{-1}$ in our calculations. However, this is another considerable source of uncertainty. In the brightest cluster galaxy RXJ0821+0752 for example, Vantyghem et al. (2017) use ^{13}CO emission to constrain the conversion factor and find it to be roughly half of the Galactic value.

The molecular mass we find for each source within the region shown on each integrated flux map is given in Table 3. In NGC 4261, we find a mass of $2.1\pm0.3\times10^7 M_\odot$. This is similar to the $2.6\pm0.4\times10^7 M_\odot$ found by Ruffa et al. (2023) when using $F_{21} = 2.14$ and $X_{CO} = 2\times10^{20}$ cm^{-2} $(K\,km\,s^{-1})^{-1}$, but is higher than the $1.1\times10^7 M_\odot$ found by Boizelle et al. (2021) with $F_{21} = 0.7$ and $X_{CO} = 3.1\times10^{20}$ cm^{-2} $(K\,km\,s^{-1})^{-1}$.

4 DISCUSSION

4.1 Velocity distribution of molecular absorption lines – evidence of cold gas inflow

In Fig. 14, we use the best-fitting central velocities to show histograms of the absorption line velocities for the galaxies shown in Figs 1–13. The top panel shows all intrinsically absorbing systems known to us with complementary high-resolution molecular emission-line observations. In the middle panel, we show the absorption regions found in galaxies possessing a molecular disc with an inclination angle of $45^\circ < i \leq 90^\circ$ (where $i = 90^\circ$ equates to an edge-on disc). In the lower panel, we show those which have no such disc. When making these histograms, we use the molecular

Table 5. The RMS noise per channel and channel width of the ALMA spectra presented in this paper. These spectra are extracted from an approximately beam sized region centred on the continuum.

Source	Line	RMS noise ($mJy\,beam^{-1}$)	Channel width ($km\,s^{-1}$)
NGC 6868	CO(1-0)	0.40	1.3
	CO(2-1)	1.44	0.6
	CN(2-1)	0.79	0.4
	HCN(2-1)	1.01	0.8
	HCO^+(2-1)	0.57	0.8
Abell S555	CO(1-0)	0.36	1.4
	CO(2-1)	1.28	0.7
	CN(2-1)	1.20	0.7
	HCN(2-1)	1.09	0.9
	HCO^+(2-1)	1.16	0.9
Hydra-A	CO(1-0)	0.77	1.4
	CO(2-1)	1.15	0.4
	CN(2-1)	0.57	0.7
	HCN(2-1)	0.49	0.5
	HCO^+(2-1)	0.46	0.5
Abell 2597	CO(2-1)	0.18	4.3
	HCN(2-1)	0.53	1.0
	HCO^+(2-1)	0.60	1.0
Abell 2390	CO(1-0)	0.22	1.9
	CO(2-1)	0.82	1.0
	HCN(2-1)	0.51	1.2
	HCO^+(2-1)	0.56	1.2
RXCJ0439.0+0520	CO(1-0)	0.59	1.9
	CO(2-1)	0.25	0.9
	CN(2-1)	0.87	0.9
	HCN(2-1)	0.87	1.2
	HCO^+(2-1)	1.03	1.2
Abell 1644	CO(1-0)	0.48	1.4
	CO(2-1)	1.13	0.7
	CN(2-1)	1.0	0.7
	CS(5-4)	1.03	0.7
	HCN(2-1)	0.85	0.9
	HCO^+(2-1)	0.87	0.9
Circinus	CO(3-2)	1.6	0.9
	HCN(4-3)	2.2	0.8
	HCO^+(3-2)	0.65	1.1
	HCO^+(4-3)	2.3	0.8
NGC 4261	CO(2-1)	0.53	5.1
	CO(3-2)	0.38	13.7
	HCN(4-3)	0.47	13.2
	HCO^+(4-3)	0.38	13.2
NGC 5044	CO(2-1)	0.78	1.3
	HCN(2-1)	0.71	0.8
	HCO^+(2-1)	0.81	0.8
NGC 1052	CO(1-0)	1.72	15.3
	CO(2-1)	0.48	20.2
	HCN(2-1)	1.74	20.2
IC 4296	CO(2-1)	0.43	1.3

Table 6. Flux density ratios and the implied excitation temperatures. RXCJ0439.0+0520 has two clearly disconnected absorption features sufficiently strong in both spectra to calculate individual excitation temperatures (the first values given are for the absorption feature at the systemic velocity). [1] For Hydra-A, we estimate the excitation temperature from the higher sensitivity HCO^+(2-1) and (1-0) observations (Rose et al. 2020).

	$\frac{\int \tau_{21}\,dv}{\int \tau_{10}\,dv}$	T_{ex} (K)
NGC 6868	$7.1^{+1.8}_{-1.8}$	-15^{+4}_{-15}
Abell S555	$9.5^{+0.8}_{-0.8}$	$-10.0^{+0.9}_{-1.1}$
Hydra-A	$3.3^{+0.2}_{-0.3}$	$^{1}11.1^{+1.4}_{-1.3}$
Abell 2390	$10.7^{+1.7}_{-1.4}$	$-8.9^{+1.1}_{-1.4}$
RXCJ0439.0+0520	$3.4^{+0.3}_{-0.3}$, $10.6^{+1.3}_{-1.2}$	48^{+44}_{-16}, $-9.2^{+0.9}_{-1.3}$
Abell 1644	37^{+17}_{-9}	$-4.1^{+0.5}_{-0.5}$
Abell 2597	>5	–
NGC 5044	>2	–
NGC 1052	$1.2^{+0.1}_{-0.1}$	$5.9^{+0.5}_{-0.5}$

species in which each source's absorption lines are best resolved. This is typically HCO^+, but is sometimes another species.[1]

In the top panel, around two-thirds of the absorption regions detected are evenly distributed within 100 km s^{-1} of the zero velocity point. The remaining third are spread across a redshifted wing between 100 and 550 km s^{-1}. The distribution of velocities is asymmetric, with the equally blueshifted side lacking any absorption regions. For edge-on or close to edge-on molecular discs, the absorption regions are spread symmetrically about 0 km s^{-1}. When excluding sources with an edge-on or close to edge-on molecular disc, the bias for redshifted absorption is particularly strong.

Due to the way absorption lines are formed, each gas cloud's direction of motion with respect to the nucleus is known without ambiguity – since an absorbing cloud must lie between the observer and the continuum, redshift (i.e. a positive velocity) indicates movement towards the galaxy centre. The only exception to this is when the relative velocity is near zero and comparable to the velocity error, typically 10–30 km s^{-1}.

The high degree of asymmetry in Fig. 14 therefore provides strong evidence of molecular gas migrating towards galaxy centres in significant quantities, particularly when excluding edge-on and close to edge-on discs. In Fig. 15, we also show the infall velocity of the absorption regions versus the velocity dispersion, as found from the Gaussian fitting procedure. This shows two distinct populations of molecular clouds. In discs, we see narrow absorption features with no net movement towards the galaxy centre. Where our line of sight does not pass through a disc, the absorption is caused by high velocity dispersion clouds. Most of these are moving towards the galactic centre along the line of sight at hundreds of km s^{-1}.

4.2 The location of absorbing molecular clouds

With the velocity distribution shown in Fig. 14, it is interesting to consider the different regions and environments within a galaxy where absorbing molecular clouds may lie, and how this would affect their properties. This is particularly important given that we lack information regarding their proximity to their galaxy's centre, even if we know their RA, Dec., and line-of-sight velocity with certainty.

In Fig. 16 we show a simplified bird's eye view of our line of sight to a galaxy with an edge-on disc of molecular gas. Perhaps the most obvious region in which clouds may lie is within the large, typically kpc scale distribution of molecular gas (which will not necessarily be a disc). We label this as region 1.

These kpc gas distributions are normally studied in ensemble via emission. However, in the Milky Way it is possible to study molecular clouds via emission on smaller mass scales due to their proximity. In the Galaxy, cold gas tends to be clumpy and assembled into clouds of 10s to 1000s of solar masses (Roman-Duval et al. 2010; Gong et al. 2016). There is also no known net flow of gas towards or away from the galaxy centre, and any orbital velocities will be perpendicular, or almost perpendicular, to our line of sight. These properties, combined with their relatively stable environment, give the clouds low line-of-sight velocities and velocity dispersions of a few km s^{-1} or less. Therefore, if the clouds we detect via absorption are from similar kpc scale distributions of molecular gas, they are likely to produce narrow absorption features with low line-of-sight velocities.

For a kpc distribution of gas, the probability of its constituent clouds aligning with the continuum is heavily dependent on our line of sight. The probability will be maximized for an edge on disc e.g. Hydra-A. In this case, any change in inclination will reduce the line-of-sight column density of molecular gas and thus reduce the chance of a cloud-continuum alignment. Therefore, when we show the absorption regions detected in edge-on or close to edge-on discs in the central panels of Figs 14 and 15, the probability that the absorption has arisen from gas within each galaxy's disc is maximized. As a result of this, there is likely to be a strong correlation between the inclination angle of a molecular disc and the number of absorbing clouds of this type – with edge-on discs like Hydra-A having the most absorbing clouds. It will likely be rare for face-on or close to face-on molecular discs to have this type of absorption.

Molecular absorption may also originate from a circumnuclear disc – a fast-rotating structure largely composed of gas and dust, which orbits the central supermassive black hole, and is typically a few pc to a few tens of pc in size. This region is labelled as '2' in Fig. 16. Although this region is of much lower mass than the galaxy-wide distribution of molecular gas, its proximity to the continuum source means an individual cloud's chance of aligning with the continuum is higher.

The circumnuclear disc is a highly energetic region which surrounds an AGN, and is composed of molecular and atomic gas. In the Milky Way for example, the circumnuclear disc has an inner radius of 1.5 pc and extends out to around 7 pc, comparable to the supermassive black hole's sphere of influence (Oka et al. 2011). Due to the highly energetic nature of this region, its molecular clouds would likely have a high velocity dispersion, which would be imprinted on to their molecular absorption lines.

A galaxy's circumnuclear disc is also typically composed of gas on elliptical orbits (Izumi et al. 2023; Solanki et al. 2023). If these are aligned such that neither the semimajor or semiminor axes are parallel to the line of sight, an apparent line-of-sight velocity can arise. In this way, elliptical orbits may induce a line-of-sight velocity of up to 200 km s^{-1} (Rose et al. 2024). However, the orientation of the orbit will rarely maximize the apparent line-of-sight velocity. Additionally, an inclination of the elliptical orbit will reduce it further by a factor of $\sin i$. Therefore, the red and blueshifted velocities induced by this will typically be 100 km s^{-1} or less. Importantly,

[1]For each galaxy, we use NGC6868 – HCO^+(2-1), Abell S555 – HCO^+(2-1), Hydra-A – HCO^+(2-1), Abell 2597 – HCO^+(2-1), Abell 2390 – HCO^+(2-1), RXCJ0439.0+0520 – HCO^+(2-1), Abell 1644 – HCO^+(2-1), Circinus – HCO^+(3-2), NGC 4261 – HCO^+(4-3), NGC 5044 – HCO^+(2-1), NGC 1052 – HCN(1-0), IC 4296 – CO(2-1), Centaurus-A – HCN(2-1).

Table 7. Column densities estimated at 5 K. The temperature used to calculate the column densities is the dominant uncertainty, so we do not give errors below.

	Absorption column density/cm^{-2}						
	CO	CO	CN	HCN	HCO$^+$	HCN	HCO$^+$
Source	(1-0)	(2-1)	(2-1)	(2-1)	(2-1)	(4-3)	(4-3)
NGC 6868	1×10^{16}	1×10^{17}	1×10^{15}	1×10^{14}	1×10^{14}	–	–
Abell S555 (absorption at ≈180 km s^{-1})	–	6×10^{15}	3×10^{14}	8×10^{13}	8×10^{13}	–	–
Abell S555 (absorption at ≈270 km s^{-1})	6×10^{15}	9×10^{16}	6×10^{14}	1×10^{14}	2×10^{14}	–	–
Hydra-A	4×10^{15}	2×10^{16}	1×10^{14}	3×10^{13}	6×10^{13}	–	–
Abell 2597	–	7×10^{16}	–	8×10^{14}	1×10^{15}	–	–
Abell 2390	6×10^{16}	1×10^{18}	–	1×10^{15}	2×10^{15}	–	–
RXCJ0439.0+0520 (absorption at ≈40 km s^{-1})	1×10^{16}	4×10^{16}	6×10^{13}	5×10^{12}	1×10^{13}	–	–
RXCJ0439.0+0520 (absorption at ≈550 km s^{-1})	1×10^{16}	1×10^{16}	1×10^{14}	2×10^{13}	1×10^{13}	–	–
Abell 1664	–	1×10^{17}	3×10^{15}	6×10^{14}	5×10^{14}	–	–
Circinus[a]	–	–	–	–	–	2×10^{14}	5×10^{14}
NGC 4261	–	–	–	–	–	1×10^{13}	4×10^{12}
NGC 5044	–	8×10^{15}	–	1×10^{13}	2×10^{13}	–	–
NGC 1052	2×10^{16}	3×10^{16}	–	–	–	–	–
IC 4296	–	1×10^{17}	–	–	–	–	–

[a]Circinus also has a CO(3-2) column density of 1×10^{17}/cm^{-2}.

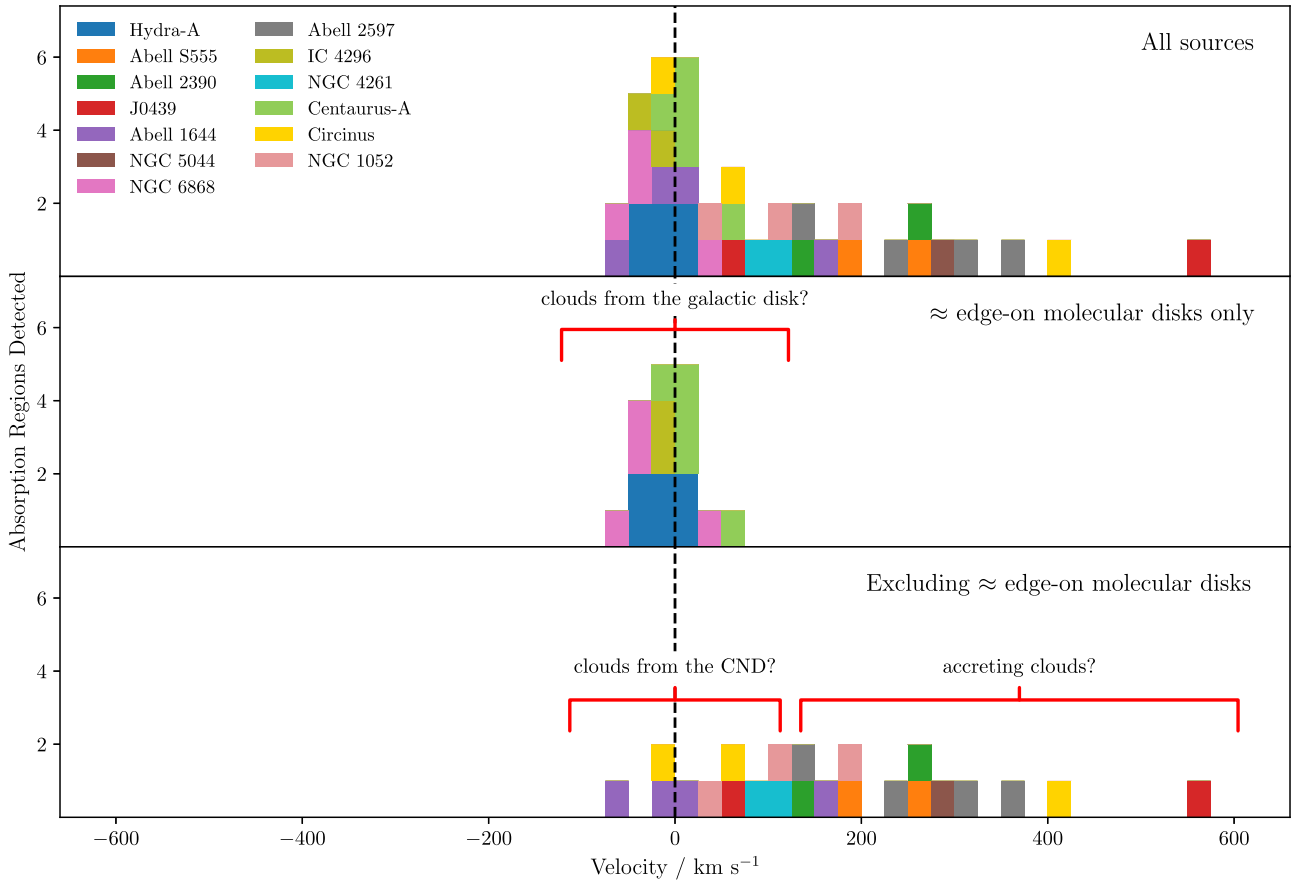

Figure 14. Upper: the velocities of all intrinsic molecular absorption regions detected (known to the authors) with complementary high-resolution molecular emission observations. The bias for positive velocities implies movement of the absorbing molecular gas towards the galaxy centres. Each galaxy's systemic velocity has an error of 30 km s^{-1} or less. Hydra-A has exceptionally high-quality data, with 12 individually resolved absorption regions. To ensure a fair comparison, for this source we show the number of individually resolved absorption regions after smoothing to 5 km s^{-1} spectral bins. **Middle**: same as above, but only for galaxies with a disc of molecular gas inclined at $45^\circ < i \leq 90^\circ$ (i.e. edge-on or close to edge-on). All absorption regions here are narrow (σ <9km s^{-1}), except one in each of NGC 6868 and Centaurus-A. **Lower:** same as upper, but excluding galaxies with a disc of molecular gas inclined at $45^\circ < i \leq 90^\circ$.

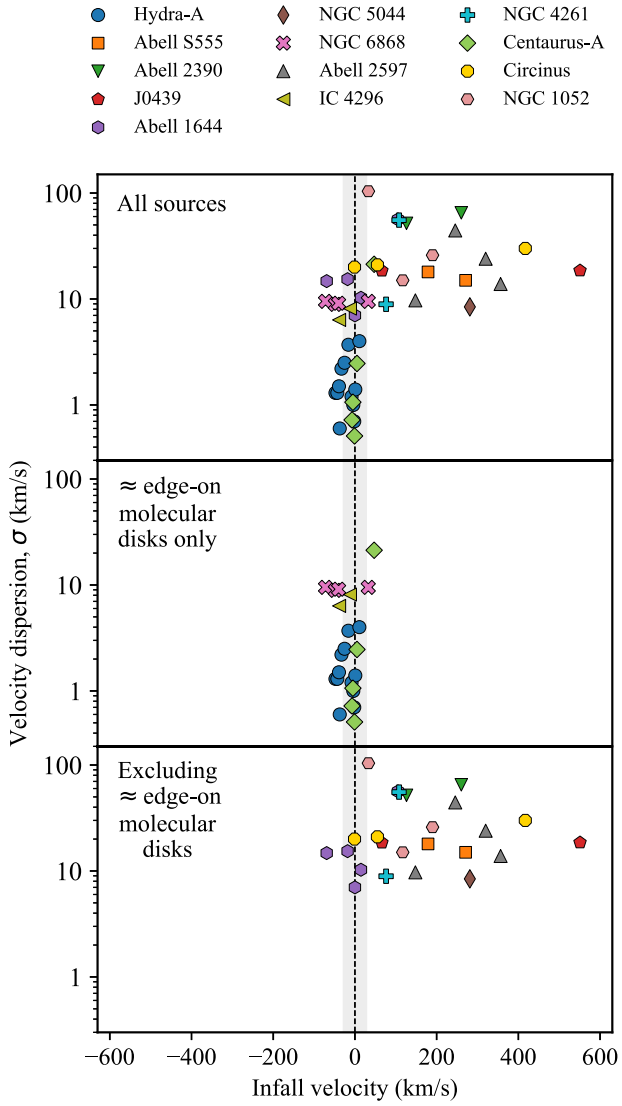

Figure 15. The infall velocity of molecular clouds versus their velocity dispersion, using the molecular line in which each system's absorption is best detected. In the top plot, we show the absorption regions detected in all sources. In the middle, we show those detected in molecular discs inclined at $45^\circ < i \leq 90^\circ$ (i.e. edge-on or close to edge-on). This orientation makes our effective line of sight through the disc as high as possible, maximizing the likelihood of absorption from its molecular clouds. At the bottom, we show absorption regions from galaxies which do not have a molecular disc inclined at $45^\circ < i \leq 90^\circ$. In these cases, there is a strong bias for redshifted absorption with high velocity dispersions. The grey band indicates the typical uncertainty in the recession velocity of each source (see Table 2).

the apparent line-of-sight velocities from this effect have an equal probability of being red or blueshifted, since the sign of the velocity simply depends on the observed direction of rotation. Therefore, the cluster of absorption regions in the lower panels of Figs 14 and 15, which have a roughly symmetric distribution of velocities between -100 and 100 km s^{-1}, are likely to be from this region.

Numerical simulations suggest that a fraction of a galaxy's molecular gas exists, at least in part, as a population of relatively small clouds within radii of a few tens to hundred of parsecs (Pizzolato & Soker 2005; Gaspari, Brighenti & Temi 2015; Gaspari et al. 2018). These clouds are expected to undergo inelastic collisions, leading to angular momentum loss and their funnelling towards

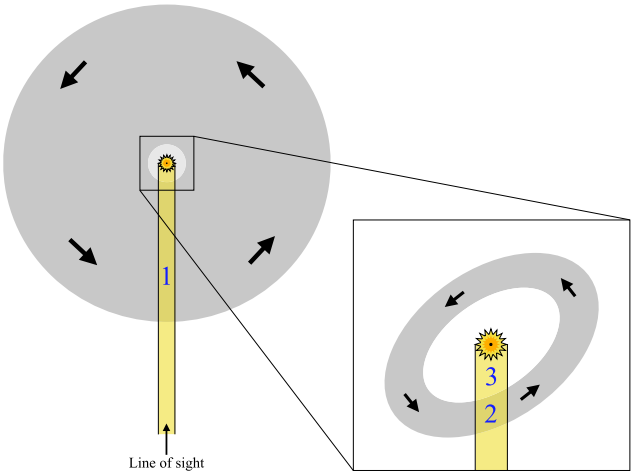

Figure 16. A bird's eye view of our line of sight to the radio continuum of an edge-on disc galaxy. Gas clouds producing molecular absorption lines may be classified as coming from three regions, as labelled above. Clouds from region 1 lie within the galaxy's kpc distribution of molecular gas, which is readily visible via molecular emission. Region 2 clouds are within the circumnuclear disc surrounding the supermassive black hole. The elliptical nature of these orbits can induce small red and blueshifted line-of-sight velocities. Clouds from region 3 originate from the circumnuclear disc and are likely falling towards the galaxy centre. This may be due to cloud-cloud collisions which have caused them to lose angular momentum. If the line of sight changes such that the galactic disc is no longer seen edge-on, the relative probability of absorption coming from regions 2 and 3 increases.

the central supermassive black hole, eventually providing it with fuel (Vollmer, Beckert & Duschl 2004). For regions with a high velocity dispersion like the circumnuclear disc, these cloud–cloud collisions are particularly likely. Therefore, regions 2 and 3 of Fig. 16 may be composed of clouds originating from the circumnuclear disc, which have undergone collisions and are migrating towards the supermassive black hole. Therefore, absorption from this region may be expected to be have a wide velocity dispersion, as well as being redshifted. To estimate the possible speeds these clouds may attain, we can consider them to be in freefall. If all the lost gravitational potential energy is converted to kinetic energy, then

$$v = \left[2GM\left(\frac{1}{r_1} - \frac{1}{r_0}\right)\right]^{0.5}, \quad (6)$$

where v is the cloud velocity after falling from stationary at a height r_0 to r_1 towards a mass M.

The exact radii at which clouds will begin to fall is uncertain. However, we can make estimates based on the size of the circumnuclear disc detected in Circinus. At the centre of the galaxy, Izumi et al. (2023) infer the presence of a 1.7×10^6 M$_\odot$ supermassive black hole (plus a molecular mass one order of magnitude lower). If freefalling from 2 to 1 pc, a velocity of 90 km s^{-1} is reached. At 0.5 pc, the velocity reaches 150 km s^{-1}. A velocity matching that of the 420 km s^{-1} HCO$^+$(3-2) absorption feature would be reached at a radius of 0.09 pc (1.9×10^4 au).

The clusters in our sample with the more massive central galaxies e.g. Abell 2390 and Abell 2597 have black hole masses around three orders of magnitude higher than Circinus. Depending on the size of the circumnuclear discs, infall may therefore be considerably faster.

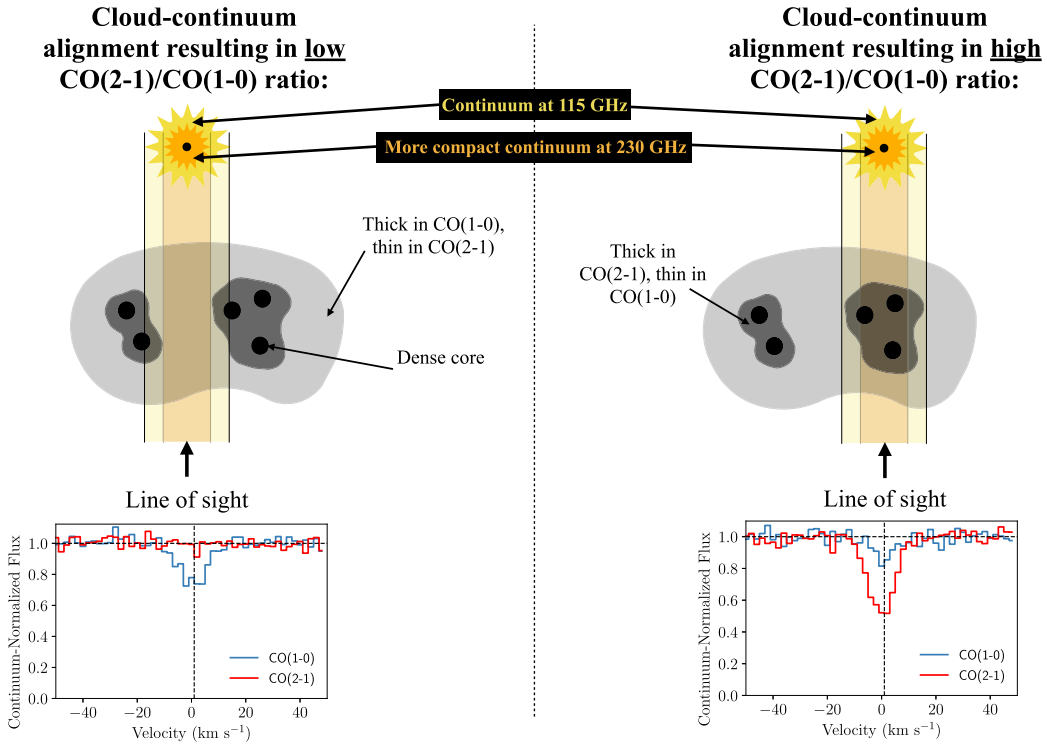

Figure 17. For a background continuum whose size varies with frequency, the relative strengths of optically thin absorption from different molecular lines may be influenced by how the cloud is positioned relative to the line of sight. Here we show the line of sight to the 115 GHz continuum in yellow, and the more compact 230 GHz continuum in orange. For the alignment on the left, our line of sight passes through no CO(2-1) thick gas, giving a low CO(2-1)/CO(1-0) ratio. For the alignment on the right, the line of sight to the 230 GHz continuum passes through a considerable column density of CO(2-1) thick gas, giving a high CO(2-1)/CO(1-0) ratio.

4.3 The fate of infalling molecular clouds

Figs 14 and 15 represent convincing evidence of cold molecular gas flowing into galactic centres at hundreds of km s^{-1}. However, the infall of these clouds may not be modelled well by freefall. Instead, with some initial angular momentum, they are likely to enter stable elliptical orbits rather than falling directly on to the supermassive black hole and providing the AGN with fuel. The radii of these stable orbits is likely extremely low, and probably sub-parsec. At this proximity to the galaxy centre, the molecular gas is likely to rapidly change into an atomic and/or ionized phase. The wide velocity dispersion of the H I gas in Abell 2597 and Abell 2390 (Figs 4 and 5) may be a manifestation of this effect, with the outer layers of the infalling clouds being evaporated and their velocity dispersion increasing. Ultimately, a fraction of the gas we see migrating towards the galactic centres may contribute to the fuelling of the AGN, with the rest likely to be ejected by radio jets and lobes in what are often seen as molecular outflows (e.g. Morganti et al. 2015; Ruffa et al. 2022; Papachristou et al. 2023) and ionized outflows (e.g. Harrison et al. 2018; Choi et al. 2020; Laha et al. 2021; Singha et al. 2021).

4.4 Cloud structure

The breakdown in our excitation temperature calculations of Section 3.1 and the resulting negative temperatures imply a false premise in our assumptions of thermodynamic equilibrium, homogeneous clouds, and a continuum source which does not change in size with frequency. However, we ruled out a lack of non-local thermodynamic equilibrium as the cause because its effect is too small. Instead, a continuum that changes in size with frequency, combined with the hierarchical structure of the molecular clouds, could explain the otherwise impossible CO(2-1)/CO(1-0) molecular line ratios.

Molecular gas concentrations are predicted to have a hierarchical structure. This consists of dense, star-forming cores up to 0.1 pc in diameter, ∼ 0.1 pc wide filaments, ∼ 1 pc wide clumps, and ∼ 1–10-pc-sized clouds (Bergin & Tafalla 2007). In Fig. 17, we show a simplified version of molecular clouds consisting of three layers: a dense core, a medium density layer, and a lower density outer layer. In the lowest density layer, there are few collisions between H_2 and CO molecules. This leaves almost all CO molecules in the ground state. Therefore, only (1-0) absorption can be produced via the promotion of molecules to the first excited state. Few molecules will be in other states, so absorption from higher order lines is not produced. The medium density layer will have more collisional excitation occurring between H_2 and CO molecules, making CO(2-1) the dominant absorption line.

Additionally, due to the 115 GHz interval in the CO(1-0) and CO(2-1) frequencies, different parts of the core may dominate at different frequencies due to spectral index variations or synchrotron opacity effects. This would produce a continuum which is smaller at higher frequencies.

On the left side of Fig. 17, we show a 230 GHz continuum which passes through only the most diffuse parts of the obscuring cloud. Since all the molecules are in the ground state, no CO(2-1) absorption is produced. The slightly larger 115 GHz continuum passes through a large volume of low-density gas, leading to strong CO(1-0) absorption. The resulting CO(2-1)/CO(1-0) ratio is very small.

On the right side of Fig. 17, we show a 230 GHz continuum which passes through a large volume of CO(2-1) thick gas. On the other hand, the volume of CO(1-0) thick gas passed through by the 115 GHz continuum is significantly lower than in the first arrangement. Thus, there is a much larger velocity-integrated optical depth ratio than the limit of 4 predicted by equation (2).

The combined effect of the molecular cloud structure and the varying size of the continuum source can therefore produce a wider range of CO(2-1)/CO(1-0) ratios than would be possible for homogeneous clouds which obscure a continuum whose size does not vary with frequency. It can also lead to apparently negative excitation temperatures.

5 CONCLUSIONS

We present analysis of intrinsic molecular absorption lines – those where the background radio continuum and the gas which absorbs it are within the same system. Our data include many new CO, CN, HCN, and HCO^+ absorption lines, as well as CO(2-1) emission. In these objects, the line's redshift unambiguously reveals the speed and direction of motion of the absorbing gas, allowing us to study its bulk motions. Our main conclusions are as follows:

(i) In galaxies where our line of sight passes through an edge-on or close to edge-on disc of molecular gas, we find low velocity dispersion clouds (typically $<9\,\mathrm{km\,s^{-1}}$) with no net inflow our outflow (Figs 14 and 15). In these respects, the clouds are similar to those seen throughout of the Milky Way. This is to be expected, given that an edge-on alignment maximizes our effective line of sight through the galaxy's disc. Therefore, the chance of the disc's molecular clouds aligning with the continuum and causing absorption is maximized.

(ii) When excluding discs, we find that absorption regions have significantly different properties. They have wide velocity dispersions (typically $>9\,\mathrm{km\,s^{-1}}$), and in terms of their line-of-sight velocities, appear to split into two groups. One has red and blueshifted line-of-sight velocities between -100 and $100\,\mathrm{km\,s^{-1}}$. We argue that these clouds are likely within the circumnuclear disc surrounding the AGNs and that their small line-of-sight velocities are a result of elliptical orbits about the galaxy centre (Fig. 16). A second group has line-of-sight velocities of around 100–550 $\mathrm{km\,s^{-1}}$, with no blueshifted counterpart. These exclusively positive velocities imply the bulk movement of molecular gas towards the galaxy centre. We interpret this as evidence of cold accretion on to the galactic centres, which is likely to contribute to AGN fuelling.

(iii) We find a wide range in the CO(2-1)/CO(1-0) ratios of the absorption regions. In around half of cases, the ratio implies a non-physical negative excitation temperature. We show that the high CO(2-1)/CO(1-0) ratios can be explained by variation in the structure of the continuum source with frequency, combined with substructure in the molecular clouds.

ACKNOWLEDGEMENTS

We are very grateful to the anonymous reviewer for their time and helpful comments, which helped us to improve the clarity of the paper. We thank Tom Oosterloo for providing the H I spectrum of NGC 6868 and Seiji Kameno for helpful discussions when analysing the ALMA data of NGC 1052. We also thank Jeff Mangum for helpful discussions on column densities. TR thanks the Waterloo Centre for Astrophysics and generous funding to BRM from the Canadian Space Agency and the National Science and Engineering Research Council of Canada. ACE acknowledges support from Science and Technology Facilities Council (STFC) grant ST/T000244/1. HRR acknowledges support from an STFC Ernest Rutherford Fellowship and an Anne McLaren Fellowship. PS acknowledges support by the Agence Nationale de la Recherche (ANR) grant LYRICS (ANR-16-CE31-0011).

This paper uses the following ALMA data: 2017.1.00629.S, 2021.1.00766.S, 2018.1.01471, 2018.1.00581, 2013.1.00229, 2012.1.00988, 2011.0.00735, 2015.1.00591, 2015.1.01290, 2013.1.01225, 2016.1.00375, 2017.1.00301, and 2017.1.01638. ALMA is a partnership of ESO (representing its member states), NSF (USA), and NINS (Japan), together with NRC (Canada), MOST and ASIAA (Taiwan), and KASI (Republic of Korea), in cooperation with the Republic of Chile. The Joint ALMA Observatory is operated by ESO, AUI/NRAO, and NAOJ. The National Radio Astronomy Observatory is a facility of the National Science Foundation operated under cooperative agreement by Associated Universities, Inc. Some of this work is based on observations carried out with the IRAM Interferometer NOEMA under project W22CK. IRAM is supported by INSU/CNRS (France), MPG (Germany), and IGN (Spain).

This research used `ASTROPY` (The Astropy Collaboration 2013, 2018), `MATPLOTLIB` (Hunter 2007), `NUMPY` (van der Walt, Colbert & Varoquaux 2011; Harris et al. 2020), `PYTHON` (Van Rossum & Drake 2009), `SCIPY` (Jones, Oliphant & Peterson 2011; Virtanen et al. 2020), and `APLPY` (Robitaille & Bressert 2012). We thank their developers for maintaining them and making them freely available.

DATA AVAILABILITY

All ALMA data presented in this paper is publicly available from the NRAO's archive.

REFERENCES

Allison J. R. et al., 2019, MNRAS, 482, 2934
Bergin E. A., Tafalla M., 2007, ARA&A, 45, 339
Boizelle B. D. et al., 2021, ApJ, 908, 19
Bolatto A. D., Leroy A., Israel F. P., Jackson J. M., 2003, ApJ, 595, 167
Bolatto A. D., Wolfire M., Leroy A. K., 2013, ARA&A, 51, 207
Braine J., Combes F., 1992, A&A, 264, 433
Choi H., Leighly K. M., Terndrup D. M., Gallagher S. C., Richards G. T., 2020, ApJ, 891, 53
Combes F., Gupta N., 2024, A&A, 683, A20
Crook A. C., Huchra J. P., Martimbeau N., Masters K. L., Jarrett T., Macri L. M., 2007, ApJ, 655, 790
David L. P. et al., 2014, ApJ, 792, 94
de Vaucouleurs G., de Vaucouleurs A., Corwin Herold G. J., Buta R. J., Paturel G., Fouque P., 1991, Third Reference Catalogue of Bright Galaxies. Springer, New York
Emonts B. H. C. et al., 2024, ApJ, 962, 187
Fabian A. C., Ferland G. J., Sanders J. S., McNamara B. R., Pinto C., Walker S. A., 2022, MNRAS, 515, 3336
Gaspari M., Melioli C., Brighenti F., D'Ercole A., 2011, MNRAS, 411, 349
Gaspari M., Brighenti F., Temi P., 2015, A&A, 579, A62
Gaspari M. et al., 2018, ApJ, 854, 167
Godard B., Falgarone E., Gerin M., Hily-Blant P., de Luca M., 2010, A&A, 520, A20
Gong Y. et al., 2016, A&A, 588, A104
Hamer S. L. et al., 2016, MNRAS, 460, 1758
Harris C. R. et al., 2020, Nature, 585, 357
Harrison C. M., Costa T., Tadhunter C. N., Flütsch A., Kakkad D., Perna M., Vietri G., 2018, Nat. Astron., 2, 198
Hernández H., Ghosh T., Salter C. J., Momjian E., 2008, in Minchin R., Momjian E., eds, AIP Conf. Proc. Vol. 1035, The Evolution of Galaxies

Through the Neutral Hydrogen Window. Am. Inst. Phys., New York, p. 214
Hunter J. D., 2007, Comput. Sci. Eng., 9, 90
Israel F. P., van Dishoeck E. F., Baas F., Koornneef J., Black J. H., de Graauw T., 1990, A&A, 227, 342
Izumi T., Wada K., Fukushige R., Hamamura S., Kohno K., 2018, ApJ, 867, 48
Izumi T. et al., 2023, Science, 382, 554
Jaffe W., McNamara B. R., 1994, ApJ, 434, 110
Jones E., Oliphant T., Peterson P., 2011, SciPy Open Source Scientific Tools for Python. Available at: www.scipy.org
Kameno S. et al., 2020, ApJ, 895, 73
Laha S., Reynolds C. S., Reeves J., Kriss G., Guainazzi M., Smith R., Veilleux S., Proga D., 2021, Nat. Astron., 5, 13
Lo K. Y., 2005, ARA&A, 43, 625
Mangum J. G., Shirley Y. L., 2015, PASP, 127, 266
Matsumoto Y., Fukazawa Y., Nakazawa K., Iyomoto N., Makishima K., 2001, PASJ, 53, 475
McMullin J. P., Waters B., Schiebel D., Young W., Golap K., 2007, in Shaw R. A., Hill F., Bell D. J., eds, ASP Conf. Ser. Vol. 376, Astronomical Data Analysis Software and Systems XVI. Astron. Soc. Pac., San Francisco, p. 127
McNamara B. R., Russell H. R., Nulsen P. E. J., Hogan M. T., Fabian A. C., Pulido F., Edge A. C., 2016, ApJ, 830, 79
Morganti R., Oosterloo T., Oonk J. B. R., Frieswijk W., Tadhunter C., 2015, A&A, 580, A1
Morganti R. et al., 2023, A&A, 678, A42
Nagai H. et al., 2019, ApJ, 883, 193
O'Dea C. P., Baum S. A., Maloney P. R., Tacconi L. J., Sparks W. B., 1994, ApJ, 422, 467
Ocaña Flaquer B., Leon S., Combes F., Lim J., 2010, A&A, 518, A9
Oka T., Nagai M., Kamegai K., Tanaka K., 2011, ApJ, 732, 120
Olivares V. et al., 2019, A&A, 631, A22
Oosterloo T., Morganti R., Murthy S., 2023, Nat. Astron., 8, 256
Papachristou M., Dasyra K. M., Fernández-Ontiveros J. A., Audibert A., Ruffa I., Combes F., Polkas M., Gkogkou A., 2023, A&A, 679, A115
Parkin T. J. et al., 2012, MNRAS, 422, 2291
Pizzolato F., Soker N., 2005, ApJ, 632, 821
Robitaille T., Bressert E., 2012, Astrophysics Source Code Library, record ascl:1208.017
Roman-Duval J., Jackson J. M., Heyer M., Rathborne J., Simon R., 2010, ApJ, 723, 492
Rose T. et al., 2019a, MNRAS, 485, 229
Rose T. et al., 2019b, MNRAS, 489, 349
Rose T. et al., 2020, MNRAS, 496, 364
Rose T. et al., 2024, MNRAS, 528, 3441
Ruffa I. et al., 2019, MNRAS, 484, 4239
Ruffa I., Prandoni I., Davis T. A., Laing R. A., Paladino R., Casasola V., Parma P., Bureau M., 2022, MNRAS, 510, 4485
Ruffa I. et al., 2023, MNRAS, 522, 6170
Singha M., O'Dea C. P., Gordon Y. A., Lawlor-Forsyth C., Baum S. A., 2021, ApJ, 918, 65
Solanki S., Ressler S. M., Murchikova L., Stone J. M., Morris M. R., 2023, ApJ, 953, 22
Tadhunter C., Oosterloo T., Morganti R., Ramos Almeida C., Villar Martín M., Emonts B., Dicken D., 2024, MNRAS, in press
Taylor G. B., 1996, ApJ, 470, 394
The Astropy Collaboration, 2013, A&A, 558, A33
The Astropy Collaboration, 2018, AJ, 156, 123
Tremblay G. R. et al., 2016, Nature, 534, 218
Tremblay G. R. et al., 2018, ApJ, 865, 13
Tully R. B., Pierce M. J., Huang J.-S., Saunders W., Verheijen M. A. W., Witchalls P. L., 1998, AJ, 115, 2264
Ursini F. et al., 2023, MNRAS, 519, 50
Van Rossum G., Drake F. L., 2009, Python 3 Reference Manual. CreateSpace, Scotts Valley, CA
Vantyghem A. N. et al., 2017, ApJ, 848, 101
Virtanen P. et al., 2020, Nat. Methods, 17, 261
Vollmer B., Beckert T., Duschl W. J., 2004, A&A, 413, 949
van der Walt S., Colbert S. C., Varoquaux G., 2011, Comput. Sci. Eng., 13, 22
Wiklind T., Combes F., 1996, Nature, 379, 139
Wiklind T., Combes F., 1997a, A&A, 324, 51
Wiklind T., Combes F., 1997b, A&A, 328, 48
Wild W., Eckart A., Wiklind T., 1997, A&A, 322, 419

SUPPORTING INFORMATION

Supplementary data are available at *MNRAS* online.

suppl_data

Please note: Oxford University Press is not responsible for the content or functionality of any supporting materials supplied by the authors. Any queries (other than missing material) should be directed to the corresponding author for the article.

This paper has been typeset from a TEX/LATEX file prepared by the author.